THESIS FOR THE DEGREE OF LICENTIATE OF ENGINEERING

Photothermal antibacterial biomaterials utilising gold nanorods and near-infrared light

MAJA UUSITALO

Department of Chemistry and Chemical Engineering

CHALMERS UNIVERSITY OF TECHNOLOGY

Gothenburg, Sweden 2024

Photothermal antibacterial biomaterials utilising gold nanorods and near-infrared light
MAJA UUSITALO

Technical report no 2024:13

Department of Chemistry and Chemical Engineering
Chalmers University of Technology
SE-412 96 Gothenburg
Sweden
Telephone + 46 (0)31-772 1000

Cover: False colour scanning electron microscopy micrograph of *Staphylococcus aureus* on gold nanorod-functionalised glass, scale bar is 200 nm.

Printed by Chalmers digitaltryck
Gothenburg, Sweden 2024

Photothermal antibacterial biomaterials utilising gold nanorods and near-infrared light

MAJA UUSITALO

Department of Chemistry and Chemical Engineering

Chalmers University of Technology

Abstract

Biomaterials serve an integral role in modern medicine, providing essential functions for therapeutic, prosthetic, and diagnostic purposes. However, once introduced into a biological setting, biomaterials are prone to bacterial colonisation, resulting in hard-to-treat infections with severe clinical consequences. Biomaterial-associated infections (BAIs) are commonly caused by biofilm-forming bacteria. The reduced sensitivity of biofilm-forming bacteria to antibiotics, along with the increased occurrence of antibiotic resistant pathogens, significantly limits the effectiveness of conventional antibacterial strategies. As our growing life expectancy is accompanied by an increased use of biomaterials, there is a pressing need for novel strategies that can combat the infections associated with these materials. A promising approach is the development of antibacterial biomaterial modifications. In this thesis, a photothermal antibacterial modification strategy using surface-immobilised gold nanorods and near-infrared (NIR) light has been investigated.

Procedures were developed for immobilisation of gold nanorods on glass and titanium substrates. Material characterisation was conducted using UV-Vis spectroscopy, electron microscopy, and X-ray photoelectron spectroscopy. In situ X-ray diffraction studies were performed to evaluate the photothermal properties of the gold nanorods on glass, and the *in situ* datasets were corroborated with scanning electron microscopy and UV-Vis spectroscopy characterisation. The findings revealed that the supported gold nanorods displayed a linear temperature increase with NIR laser power until an onset of morphological changes around 120 °C, and the slope of the temperature increase demonstrated a dependence on the surface coverage of gold nanorods. The in vitro antibacterial activity of the gold nanorods on glass and titanium upon illumination with NIR light was evaluated against Staphylococcus aureus. On titanium, the antibacterial activity was attributed to NIR light absorption of the titanium leading to heating of the substrate, with no evident effect from plasmonic heating of the gold nanorods. In contrast, on glass a significant NIR light-intensity dependent antimicrobial activity from plasmonic heating of the gold nanorods was observed. The findings provide insights into the photothermal behaviour of surface-immobilised gold nanorods and highlight the important role of the support material for the antibacterial activity of the systems. Altogether, the results are of relevance for advancing the design of antibacterial biomaterial modifications using supported gold nanorods and near-infrared light.

Keywords: biomaterial-associated infections, photothermal therapy, gold nanorods, near-infrared light

List of publications

Paper I

Development of biomaterial modifications with antibacterial efficacy using gold nanorods and near-infrared light

Maja Uusitalo, Gustav Eriksson, Mats Hulander, Martin Andersson

Manuscript

Paper II

Photothermal properties of supported gold nanorods

Maja Uusitalo[‡], Michal Strach[‡], Gustav Eriksson, Tetiana Dmytrenko, Mats Hulander, Martin Andersson

Manuscript

[‡] The authors contributed equally to this work

Contribution report

Paper I: Main author. Performed all experiments and analyses except for TEM characterisation and XPS measurements. Wrote the first draft of the manuscript.

Paper II: Shared main author. Performed syntheses, sample preparation, and sample characterisation (UV-Vis, SEM). Co-wrote the first draft of the manuscript.

Abbreviations

AuNR	Gold nanorod
BAI	Biomaterial-associated infection
CFU	Colony forming unit
CTAB	Hexadecyltrimethylammonium bromide
Glass-AuNR	Gold nanorods supported on glass
LSPR	Localised surface plasmon resonance
NIR	Near-infrared
PTT	Photothermal therapy
SEM	Scanning electron microscopy
TEM	Transmission electron microscopy
Ti-AuNR	Gold nanorods supported on titanium
UV-Vis	Ultraviolet-visible
XPS	X-ray photoelectron spectroscopy
XRD	X-ray diffraction

Table of contents

Abstract I
List of publications II
Abbreviations III
Table of contents IV
1. Introduction 1
2. Background 3
2.1 Antibacterial modifications of biomaterials 3
2.2 Photothermal therapy 3
2.3 Gold nanoparticles and their biomedical applications 4
2.3.1 Gold nanorod synthesis 5
2.3.2 Photothermal therapy using gold nanorods 6
2.3.3 Nanothermometry of gold nanoparticles 7
3. Methodology 9
3.1 Material preparation 9
3.1.1 Gold nanorod syntheses 9
3.1.2 Gold nanorod surface-immobilisation 9
3.2 Material characterisation 10
3.2.1 Electrophoretic and dynamic light scattering 10
3.2.2 Transmission electron microscopy 10
3.2.3 UV-Vis spectroscopy 10
3.2.4 Scanning electron microscopy 11
3.2.5 X-ray photoelectron spectroscopy 11
3.3 *In situ* X-ray diffraction 11
3.4 Antibacterial activity 13
4. Results and discussion 15
4.1 Material characterisation 15
4.1.1 Gold nanorods 15
4.1.2 Gold nanorod-functionalised materials 17
4.2 Evaluation of photothermal properties 20
4.2.1 Theory: heating of plasmonic nanoparticle arrays 20
4.2.2 *In situ* X-ray diffraction 20
4.2.2.1 Conventional heating 22
4.2.2.2 NIR laser heating 25
4.3 Antibacterial activity 26
4.3.1 Gold nanorod-functionalised titanium 26
4.3.2 Gold nanorod-functionalised glass 27

5. Concluding remarks 31
6. Future perspectives 33
Acknowledgements 35
References 37

1. Introduction

Humans today live longer than ever. Over the last decades, the global life expectancy has seen a continuous increase, which is a trend that is projected to continue [1]. This progress is the result of a wide range of contributing factors, including improved hygiene, living conditions, and access to essential health services. A significant role is also played by the remarkable advancements within medicine and healthcare, and we currently have treatment strategies for a range of diseases and physical injuries that some decades ago were not imaginable. The discovery and development of new drugs has been a crucial part of the advancement of modern medicine, with the introduction of antibiotics serving as the most significant example. In addition to treating infectious diseases, antibiotics have facilitated a range of medical procedures, making their impact on the medical field far-reaching. Although the development of new drugs like antibiotics has been essential, the important impact on modern medicine from advancements in materials science providing us with new and improved biomaterials should not be overlooked. A biomaterial can broadly be defined as a material used in contact with living tissues, organisms, or microorganisms [2]. Biomaterials can be natural or synthetic and are used to repair, augment, or replace damaged tissue or a biological function. The use of biomaterials encompasses a variety of applications, including medical implants like joint prostheses, heart valves and dental implants, and other medical devices such as urinary catheters, sutures, and staples.

As apparent from their widespread application, the use of biomaterials is central within medicine, providing essential functions for therapeutic, prosthetic, and diagnostic purposes. Nonetheless, there are still challenges in regard to their practical implementation, with the most common being biomaterial-associated infections (BAIs). The surface of a biomaterial is designed to interact favourably with the macromolecules and cells of our own body; however this property also makes it a potentially favourable environment for bacterial adhesion. Bacterial colonisation, proliferation and subsequent biofilm formation on a biomaterial surface causes hard-to-treat infections with severe clinical consequences. The infection incidence varies greatly depending on the function and location of the biomaterial, from 1-2% in hip and knee prosthesis, up to 30% for indwelling urinary catheters [3,4]. Currently, prevention and treatment strategies for these infections include conventional antibiotics, and when applicable, revision surgery with debridement or removal of the implanted material. In addition to severe discomfort for patients and high societal costs, the risk of reinfection after revision surgery is considerable [4].

While the use of antibiotics is essential for infection prevention and treatment, bacterial biofilms exhibit increased tolerance to antibiotics [5], making them very difficult to eliminate. Furthermore, the problem is aggravated by the increasing occurrence of antibiotic resistant pathogens [6], limiting the effectiveness of many conventional drugs. As our growing life expectancy is accompanied by an increasing use of biomaterials, we are now faced with a pressing need for novel strategies in combatting the infections associated with these materials.

An alternative approach to combatting BAIs is developing modifications of the biomaterial that provide it with antibacterial properties. These properties can be attained through a range of

strategies, which either actively eradicate bacteria like in designing contact-killing surfaces and antimicrobial-releasing coatings, or prevent bacterial colonisation through the use of non-adhesive (antifouling) surfaces [4]. Advancements in nanotechnology have had a significant role in the development of these antibacterial strategies. The unique properties of nanomaterials provide a wide range of possibilities, including the introduction of nanotopography to prevent bacterial adhesion, and harnessing the bactericidal properties of various nanoparticles [7]. In this thesis, an antibacterial modification strategy using photothermal gold nanorods activated by near-infrared (NIR) light has been investigated.

This aim of this thesis was to develop and evaluate a photothermal antibacterial biomaterial modification strategy based on supported gold nanorods excited with NIR (808 nm) light. For this purpose, material preparation protocols for the surface-immobilisation of gold nanorods on glass and titanium were developed, and the produced materials' properties were evaluated. The two main focuses of the thesis were assessing the materials' photothermal characteristics using *in situ* X-ray diffraction (gold nanorods on glass), and *in vitro* antibacterial activity (gold nanorods on glass and titanium).

2. Background

The following sections provide the relevant theoretical background concerning the concepts, materials, and characterisation techniques included in the thesis. Initially, an overview of the modification strategies employed in the development of antibacterial biomaterial modifications is given, followed by an introduction to photothermal therapy. Thereafter, the properties and synthesis of gold nanoparticles are explained. Finally, a summary of nanothermometry methods developed to determine the temperature of gold nanoparticles is provided.

2.1 Antibacterial modifications of biomaterials

The need for alternatives to conventional antibacterial agents like antibiotics in combatting BAIs has led to a great interest in the development of antibacterial modifications of biomaterials. The development of such antibacterial modifications is a considerable challenge due to the complexity of finding a strategy that fulfils all the necessary requirements. The biomaterial modification should not only provide an antibacterial activity against a range of microorganisms, but also not be harmful the local immune competence or surrounding tissue. Depending on the biomaterial type, the modification should furthermore not influence the biomaterial's innate tissue integrative properties. Taking this into consideration, it is clear that there is no universal modification strategy, and the importance of considering the specific requirements for each biomaterial application is highlighted.

The strategies developed to achieve an antibacterial functionality of a biomaterial can broadly be divided into contact-killing surfaces, antimicrobial-releasing materials, non-adhesive (or antifouling) surfaces, or a combination of the above [4]. Examples of contact-killing surface modifications include immobilisation of quaternary ammonium compounds and antimicrobial peptides. For antimicrobial-releasing systems the active compound can either be incorporated in the bulk, e.g. by addition during material preparation or adsorption in permeable materials, or in a coating on the biomaterial. An array of antimicrobial substances has been integrated in the release-systems, including conventional antibiotics, silver, and antimicrobial peptides [7]. Non-adhesive modifications include various polymer or polymer brush coatings, as well as superhydrophobic surfaces obtained by tuning surface roughness. As a part of these broad categories of antibacterial modifications, strategies exist that use surfaces or coatings that exhibit a photoinduced antibacterial activity. Examples of such photoactive surfaces are titanium oxide that when irradiated with suitable photon energies produces reactive oxygen species [7], and materials with immobilised photothermal agents, like plasmonic nanoparticles, which generate heat when irradiated with resonant light [8].

2.2 Photothermal therapy

In photothermal therapy (PTT), photothermal agents that convert light energy into heat are used to treat a medical condition. Photothermal therapy has been extensively studied as a cancer treatment approach, wherein light is used as an external stimulus to achieve controlled and confined thermal damage to tumour tissue. However, photothermal therapy has also been investigated for applications beyond cancer therapy, for example in treating bacterial infections. The principle behind the therapy approach is that light absorption of photothermal agents leads to electron excitation, and when the electronic excitation energy relaxes through

nonradiative decay, heating of the local environment around the absorbing agent occurs [9]. If the photothermal agent is introduced in vicinity of the targeted group of cells, the heat released upon irradiation can induce thermal damage, generally through cell membrane disruption and protein denaturation.

The photothermal agents employed in PTT can be for example natural chromophores in tissue, photoabsorbing dyes [9], or nanomaterials like polymer nanoparticles, carbon nanotubes, or plasmonic metal nanoparticles [10]. As natural chromophores exhibit very low light absorption and dye molecules suffer from photobleaching under laser irradiation, the use of nanomaterials has emerged as a suitable alternative to overcome these limitations. For *in vivo* photothermal therapy, using near-infrared (NIR) light around 650-900 nm is preferable, as these wavelengths exhibit optimal tissue penetration due to minimal absorption by water and haemoglobin [11]. Several nanomaterials exhibit light absorption in this spectral region and thus have potential as photothermal therapy agents. However, using plasmonic gold nanoparticles is especially promising due to their ease of preparation, large absorption cross-sections, and ready (bio)functionalisation [9]. Furthermore, gold nanoparticles have tuneable optical properties, which allow their light absorption to be tuned to specific wavelengths in the NIR region by changing the size and shape of the particles.

2.3 Gold nanoparticles and their biomedical applications

Over the last decades, the research interest in gold nanoparticles has seen a continuous increase and they have found application within a wide range of research areas including sensing, imaging, catalysis, PTT, and drug delivery [12]. However, utilising the unique properties of gold nanoparticles it not a modern phenomenon, but something that has been done for centuries, for example in producing the vibrant colours of stained-glass windows in medieval churches. Naturally, these early applications were without understanding the phenomenon causing the observed colours. It was first in the mid-19th century when Michael Faraday began examining the interaction between light and metal particles that scientists started to study the topic [13]. Nowadays, we have a good understanding of the origin of the unique properties of gold nanoparticles, facilitating their practical implementation.

When the dimensions of a material are reduced to the nanoscale (1-100 nm), the small size and high surface-to-volume ratio make new properties manifest, stemming from the spatial confinement imposed on the materials' electronic motion. For gold and other noble metal (plasmonic) nanoparticles, their interesting optical properties are caused by unique interactions with light. In the presence of the oscillating electromagnetic field of light, a coherent oscillation of the conduction band electrons of the gold nanoparticle with respect to the positive metal lattice takes place [14]. This coherent oscillation is resonant at a specific frequency of light and is called localised surface plasmon resonance (LSPR). Resonant photons can thus be confined within the gold nanoparticle and excite the LSPR oscillations, and the plasmonic confinement results in a great enhancement in properties like light absorption, light scattering, and fluorescence [15]. Following excitation, the LSPR oscillations decay through radiative processes giving rise to photon emission, or through nonradiative processes resulting in the emission of heat [15]. By exposing a gold nanoparticle to resonant light it can thus strongly absorb the light and convert it into heat, making them efficient photothermal agents.

The LSPR frequency depends on the size and shape of the gold nanoparticle, as well as the dielectric constant of the surrounding medium, making it possible to tune where the nanoparticle absorbs light and the excitation of the LSPR occurs. Spherical gold nanoparticles exhibit one LSPR frequency due to their symmetrical shape, and in water their absorption maximum lies in the visible part of the electromagnetic spectrum around 500 nm. By changing the shape of the gold nanoparticle from spherical to rod-shaped, it will exhibit two resonances: one transverse associated with oscillations along the short axis, and one longitudinal associated with oscillations along the long axis (Fig. 1) [15]. The longitudinal LSPR frequency is strongly dependent on the aspect ratio (length/width) of the gold nanorod, and by increasing the aspect ratio it is shifted from the visible to NIR region.

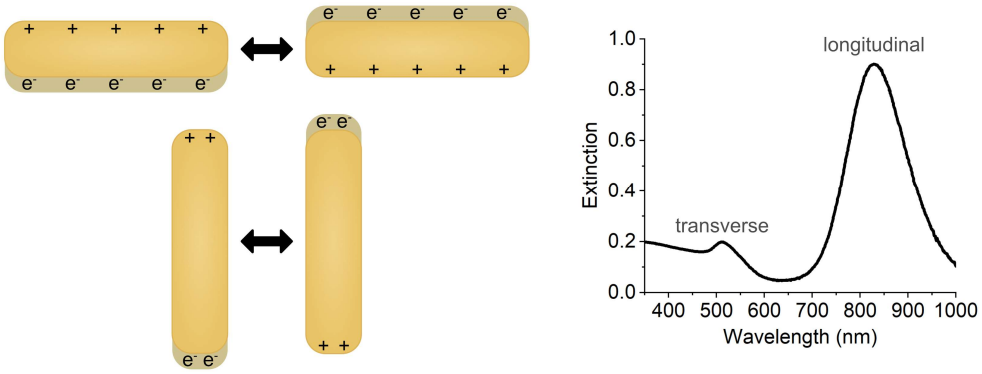

Fig. 1. Schematic illustration of the transverse and longitudinal localised surface plasmon resonance (LSPR) oscillations of a gold nanorod induced by the electric field of incident light, and the two associated LSPR bands in the visible and near-infrared spectral region.

2.3.1 Gold nanorod synthesis

As the properties of gold nanoparticles are affected by their size and shape, much effort has been spent on developing reproducible and scalable synthesis protocols yielding nanoparticles of narrow size and shape distributions. Gold nanoparticles are commonly synthesised via bottom-up, wet-chemical procedures, with one well-known example being the Turkevich method for synthesis of gold nanospheres. In the Turkevich method, an aqueous solution of gold(III) chloride trihydrate ($HAuCl_4$) is reduced by citrate under boiling [16], wherein the citrate works both as the reducing agent for the gold salt and as a stabilising ligand on the formed nanoparticles. Transitioning from synthesising spherical to rod-shaped gold nanoparticles requires achieving preferential reduction of gold ions onto certain crystal facets of the nanoparticle, tuning the growth rates so that the particle grows faster in one direction.

For synthesising gold nanorods, a seed-mediated synthesis in the presence of hexadecyltrimethylammonium bromide (CTAB) and silver is the most popular approach due to its simplicity, ease of particle size control and high quality and yield [15]. It is a two-step synthesis where (1) a seed suspension is made by reducing $HAuCl_4$ in the presence of CTAB with sodium borohydride, and (2) the spherical seed particles are added to a growth solution containing Au^+ ions in the presence of CTAB and silver nitrate, which is obtained by reduction

of $HAuCl_4$ with ascorbic acid. Ascorbic acid can only reduce the Au^+ to Au^0 in the presence of the gold seed particles that catalyse the reduction [17], meaning that deposition of gold onto the existing seeds will occur, causing them to grow in size eventually forming single-crystalline gold nanorods. The CTAB used in the synthesis works as a stabilising ligand capping the nanoparticles and also has an important shape-directing role, while the silver ions are important in facilitating rod-formation and controlling the aspect ratio. In this thesis, the seed-mediated synthesis using CTAB and silver nitrate was used to synthesise gold nanorods with longitudinal resonance bands in the NIR region around 825-850 nm.

The growth mechanism of single-crystalline gold nanorods has been a discussed topic, with multiple mechanisms proposed. The key elements are that CTAB molecules preferentially bind to the {110} side facet of the nanoparticle. Ag^+ ions are reduced to Ag^0 at the gold nanoparticle surface (through underpotential deposition) and the deposition of Ag^0 is faster on the side {110} facet than on the end {100} due to a lower reduction potential on the {110} facet. Silver deposition and CTAB binding to the {110} facet thereby inhibits growth on the sides, resulting in preferential growth at the ends along the [110] direction into a rod-shape [15].

2.3.2 Photothermal therapy using gold nanorods

By synthesising gold nanorods of suitable aspect ratio their LSPR excitation frequency, and by extension their photothermal heating, can be tuned to the NIR region. As gold nanorods provide the benefit of using light in this spectral range for extracorporeal excitation and heat generation, they have been employed for a range of photothermal therapy applications, including therapy of different types of cancer cells [18,19] and bacterial infections [20,21]. For photothermal cancer therapy relying on systemic administration of gold nanorods, the particles are commonly functionalised in order to improve stability and to achieve targeting specificity.

Functionalisation strategies employed include utilising ligands, like antibodies, specific to biomarkers on the targeted cells, and passivating the particles with polyethylene glycol (PEG). PEG functionalisation improves the biostability of the gold nanorods, preventing aggregation, and for *in vivo* applications PEGylated nanoparticles are accumulated in tumour tissue due to the enhanced permeability and retention effect [9]. Through this, the PEGylation works as a passive targeting approach towards the tumour cells, in comparison to the active targeting using antibodies. As a treatment approach for bacterial infections, similar active targeting strategies have been investigated, wherein the gold nanorods were conjugated with ligands or antibodies specific to moieties in the bacterial cell membrane [20,21].

However, the systemic administration approach faces certain challenges. Active targeting using antibodies can be negated by the formation of a protein corona *in vivo*, and passive targeting relying on the enhanced permeability and retention effect has been shown to be rather inefficient [22]. As previously mentioned, the photothermal properties of plasmonic nanoparticles have also been utilised in the development of antibacterial modifications of biomaterials. By immobilising gold nanorods on a biomaterial surface, some of the challenges faced when using systemic administration can be overcome and the therapy approach becomes more suitable for combatting BAIs. The gold nanorod-functionalised surface can provide a

light-activated, broad-spectrum, local antibacterial activity at the site of the bacterial colonisation, while simultaneously ensuring the nanoparticles' stability.

Using the photothermal properties of surface-immobilised gold nanorods to obtain antibacterial biomaterials is something that has been studied on a range of materials, including titanium [23], polypropylene [24], polyurethane [8], and glass [25,26]. These works have shown that surface-immobilised gold nanorods can provide an antibacterial activity against several bacterial species upon irradiation with NIR light. The materials from past studies have used gold nanorod loadings ranging from a couple of hundred nanoparticles per μm^2 to complete multilayer coatings, and the antibacterial activity has been evaluated mainly for low laser intensities as a function of irradiation time.

To further investigate and understand the photothermal antibacterial activity of supported gold nanorods, this thesis studied gold nanorods surface-immobilised in well-defined monolayers on both glass and titanium. The antibacterial efficacy of the developed materials was evaluated as a function of NIR light intensity, and the role of the support material has been examined.

2.3.3 Nanothermometry of gold nanoparticles

For applications utilising the photothermal properties of plasmonic nanoparticles such as gold nanorods, the question of the nanoparticles' temperature is of great relevance. However, as the heat that is generated from a gold nanoparticle irradiated with resonant light is spatially confined on the nanoscale, determining the temperature of these systems is a non-trivial task. A range of methodologies have been developed for experimental determination of the local temperature increase caused by the excitation of gold nanoparticles with resonant light. Many of the methods evaluate the temperature by measuring some change in property in the surroundings of the gold nanoparticles. This has for example been achieved by introducing fluorescent molecular probes [27,28] and upconverting nanoparticles [29] in the close vicinity of the particles, by using the phase transition of lipid bilayers and measuring the melted area around the particles [30,31], and by monitoring changes in refractive index or viscosity in the surrounding medium [32,33]. While these approaches have shown good accuracy and temperature determination in a rather wide range, they are limited by the fact that only the temperature in the close proximity of the gold nanoparticle can be assessed. Moreover, many techniques in literature rely on optical detection, placing limitations on the spatial resolution due to the diffraction limit of visible light [34].

An alternative temperature determination approach that has been explored utilises the lattice expansion associated with heating of the gold nanoparticles. With X-ray diffraction (XRD) it is possible to monitor shifts and shape changes in the Bragg peaks of the crystalline gold nanoparticles as they are excited by resonant light, and from this determine their exact temperature as well as monitor potential structural changes occurring in the particles. This approach has previously been employed at synchrotron facilities using pulsed laser excitation of spherical gold nanoparticles in water [35] and on silicon substrates [36]. The studies have shown the effectiveness of the method and evaluated the temperature increase of the nanoparticles as a function of laser power, pre-melting and recrystallisation of the particles, and heat-transfer to the support material. In this thesis, the approach is extended to evaluate the

photothermal characteristics of the more biologically relevant system of gold nanorods supported on glass substrates upon excitation with NIR light.

3. Methodology

The following sections describe the material preparation and characterisation covered in this thesis. The methodology for the evaluating the photothermal properties of the supported gold nanorods using *in situ* XRD is summarised and an overview of the antibacterial activity evaluation is given. The NIR laser utilised in the thesis had a central wavelength of 808 ± 3 nm (BWT Beijing Ltd., model DS3-51523-50.00W). The laser was connected to an air-spaced doublet collimator (F810SMA-780, Thorlabs) and a 2X beam expander (GBE02-B, Thorlabs). More detailed material and procedure descriptions are available in Paper I and Paper II appended to the thesis.

3.1 Material preparation

3.1.1 Gold nanorod syntheses

Two different aspect ratios of gold nanorods (AuNRs) were synthesised, one with an average aspect ratio of 3.9 (AuNR 3.9) and one with an average aspect ratio of 4.4 (AuNR 4.4). In Paper I, only the 3.9 aspect ratio gold nanorods were used and is referred to as simply "AuNR".

The gold nanorod synthesis protocols were adapted from a seed-mediated synthesis procedure described elsewhere [17]. The seed-mediated synthesis involves firstly preparing a seed suspension consisting of small ($d < 5$ nm) single-crystalline gold nuclei. Briefly, 25 µl of 50 mM gold(III) chloride trihydrate ($HAuCl_4$) solution was added to 4.7 ml of 100 mM CTAB solution in a 30 °C water bath. Thereafter, 300 µl of freshly prepared sodium borohydride solution was added under strong stirring.

For synthesising the 3.9 aspect ratio AuNRs, a growth solution was prepared in a 30 °C water bath by adding 1.14 ml 1 M hydrochloric acid and 600 µl of 50 mM $HAuCl_4$ solution to 60 ml 100 mM CTAB solution. Subsequently, 720 µl of 10 mM silver nitrate and 600 µl of 100 mM ascorbic acid solution was added, completing the growth solution. Lastly, 144 µl of the seed suspension was added to the growth solution, thoroughly mixed, and then left undisturbed at 30 °C for 1 h and 50 min. To obtain the 4.4 aspect ratio AuNRs, the same procedure was utilised, but the silver nitrate and ascorbic acid concentration in the growth solution was adjusted to 11 mM and 90 mM, respectively. Furthermore, the growth time for the 4.4 aspect ratio AuNRs was extended to 2 h.

The synthesised gold nanorods were purified from their reaction mixture by three repeated centrifugations, in which the gold nanorods were redispersed in ultrapure water in between each centrifugation step. Once purification was complete, the stock AuNR suspensions were stored at 4 °C protected from light.

3.1.2 Gold nanorod surface-immobilisation

The gold nanorods were immobilised onto two different substrates: glass coverslips (⌀ 13 mm, #1.5, VWR) and titanium discs (⌀ 9 mm). In Paper I, both support materials are included as support for the AuNR 3.9 and referred to as Glass-AuNR and Ti-AuNR. In Paper II, only glass was used as support for the two morphologies of AuNRs evaluated (AuNR 3.9 and 4.4).

The immobilisation was based on electrostatic interaction between the positively charged AuNRs and negatively charged support surfaces. The glass and titanium substrates were rinsed with 95% ethanol followed by ultrapure water before being dried with nitrogen gas. The pre-treatment of the substrates conducted to achieve the negative surface charged varied depending on the material. The glass substrates were immersed in nitric acid (65-67%) overnight (18-19 h), whereafter they were rinsed thoroughly with ultrapure water before being immersed in an AuNR suspension. The titanium substrates were treated with UV/O_3 for 15 min, whereafter they were immersed in an AuNR suspension. The surface coverage of AuNRs on the substrates was varied by adjusting the concentration of the AuNR suspension and the immersion time. The concentration of the AuNR suspensions was estimated in terms of weight of gold per volume (μg/ml) from the absorbance value at 400 nm, based on a correlation described elsewhere [17]. After the AuNR immersion was completed, the AuNR suspension was exchanged to ultrapure water before the substrates were removed, immersed in 99.5% ethanol, and finally allowed to air dry.

3.2 Material characterisation

3.2.1 Electrophoretic and dynamic light scattering

For Paper I, the surface charge of the AuNR 3.9 was estimated by measuring the electrophoretic mobility of the nanoparticles. Electrophoretic light scattering (ELS) and dynamic light scattering (DLS) was performed using a Litesizer DLS 500 from Anton Paar. The stock AuNR suspension was diluted to an estimated gold concentration of 15 μg/ml with ultrapure water. The measurements were run at 25 °C, the angle used for DLS was 175°, and both ELS and DLS measurements were repeated three times.

3.2.2 Transmission electron microscopy

Transmission electron microscopy (TEM) was performed to determine the dimensions and crystal structure of the synthesised AuNRs. TEM is a high-resolution electron microscopy technique wherein a thin sample (< 100 nm) is exposed to a high-energy electron beam and characteristic signals (secondary electrons, back-scattered electrons, characteristic X-rays) that are transmitted through the sample are detected. In this thesis, bright-field imaging was used to evaluate the morphology and phase contrast of the samples.

TEM samples were prepared by placing 5 μl droplets of diluted AuNR suspension (25 μg/ml gold concentration) onto UV/O_3-treated copper grids with an ultrathin carbon film on a lacey carbon support film (TED Pella). Excess AuNR suspension was removed by blotting the grid with filter paper. TEM characterisation was performed using a FEI Titan 80-300 operated in TEM mode at 300 kV. The obtained TEM micrographs were analysed using GATAN Microscopy Suite 3 and the image analysis software Fiji (ImageJ). The AuNR dimensions (length, width, aspect ratio) were determined by measuring a total of 400 nanoparticles for each morphology.

3.2.3 UV-Vis spectroscopy

The optical properties of the synthesised AuNR suspensions as well as the AuNRs supported on glass were characterised with UV-Vis spectroscopy. Characterisation was performed using

a Multiskan GO Microplate Spectrophotometer for the AuNR suspensions and for the samples of AuNRs supported on glass while immersed in water. The absorption spectra of the AuNRs supported on glass in air was measured by placing the samples in the light path of a Hewlett Packard 8453 spectrophotometer. Absorption spectra were measured in the wavelength range of 400-1000 nm.

3.2.4 Scanning electron microscopy

Scanning electron microscopy (SEM) was used to image the AuNRs supported on glass and titanium. In SEM, a focused electron beam is scanned across an area of the sample and in each position characteristic signals (secondary electrons, back-scattered electrons, characteristic X-rays) generated by interactions between the electron beam and the sample are detected. In this work, secondary electron detection was used to obtain micrographs with topographic information. SEM was performed using a Zeiss Ultra 55 scanning electron microscope. AuNR-functionalised glass and titanium samples were imaged in secondary electron mode with acceleration voltage 2-5 kV. The SEM micrographs were analysed with respect to surface coverage of AuNRs (percentage projected area covered by AuNRs).

SEM was further used to study the bacteria-material interaction on the samples from the *in vitro* antibacterial activity evaluation. The samples were fixated in 4% formaldehyde (VWR) for 90 min before being dehydrated by stepwise immersion in an ethanol gradient. After dehydration, the samples were transferred to a solution of 50% v/v hexamethyldisilazane (HDMS) in ethanol and left for 15 min. Lastly, a final immersion in 100% HDMS for 15 min was performed before the samples were air-dried. Prior to SEM characterisation, the samples were sputter coated with approximately 5 nm of gold.

3.2.5 X-ray photoelectron spectroscopy

X-ray photoelectron spectroscopy (XPS) was performed for paper I to characterise the surface chemical composition of the AuNR 3.9 supported on glass and titanium. XPS is a surface sensitive technique where the sample is exposed to monochromatic X-rays and the kinetic energies of emitted photoelectrons are measured. The characteristic photoelectrons emitted from the sample surface provide information on the electronic states of the atoms. XPS was performed to determine the chemical composition of the AuNR-functionalised glass and titanium samples, before and after the UV/O_3-treatment conducted as a sterilisation step prior to the *in vitro* antibacterial activity evaluation. Focus was placed on the amount of gold and silver in the samples, providing information regarding the AuNRs, as well as the amount of carbon before and after UV/O_3-treatment, as an indicator of CTAB removal from the surface of the AuNRs. XPS was conducted using a Versaprobe III spectrometer (PHI) with monochromated Al Kα radiation. A 100 x 100 μm spot size on the samples was illuminated by the X-ray beam.

3.3 *In situ* X-ray diffraction

In paper II, the photothermal properties of the AuNRs supported on glass upon irradiation with NIR light were evaluated with *in situ* X-ray diffraction (XRD). In XRD, an incident monochromatic X-ray beam is scattered by the regularly arranged atoms in the sample, and

constructive interference between the scattered X-rays occurs when conditions satisfy Bragg's law. By detecting the intensity of the scattered beam through a range of 2θ-angles (angle between incident and scattered beam), the diffraction peaks in the resulting diffractogram can give information about crystal structure and chemical composition. Here, XRD was used to monitor shift and shape-changes in the Bragg peaks of the AuNRs supported on glass caused by heating of the nanoparticles.

Furnace heating experiments were performed to determine the thermal expansion coefficient for the AuNRs and to evaluate how conventional heating influence the morphology of the supported AuNRs. The main series of furnace heating experiments were performed on a D8 Advance X-ray diffractometer (Bruker) using a Cu X-ray source, position-sensitive detector, and variable slit set to 6 mm sample length. The instrument was equipped with a XRK900 heating chamber (Anton Paar). As-prepared samples were placed on a Macor ceramic support inside of the heating chamber. Temperature calibration was performed using MgO powder deposited on the same glass substrate as the AuNRs. The displacement due to thermal expansion was determined from a series of Z-scans using the same temperature ramp. Data for the AuNRs was corrected accordingly, for the sample displacement error and temperature readout error. The evolution of the (200) Au peak was monitored with 10-20 min scans in the 2θ range 42-46°, wherein the scan times depended on the signal-to-noise ratio. Heating ramps were 0.1°/s and the samples were equilibrated for 30 min at each set temperature.

A complementary series of measurements were conducted on a SaxsLab MAT:Nordic system equipped with a microfocus Cu source and Pilatus 300K (SAXS) and 100K (WAXS) detectors from Dectris. A Linkam HFSX350 heating stage was used for heating and the temperature was calibrated with MgO powder. The configuration provides less peak position accuracy but better signal-to-noise ratio due to the focusing X-ray source and large 2D detector, as well as higher temperature accuracy. Experiments were performed with the entire beam path under vacuum, and the heating stage was mounted at a 22° angle to the incident beam to fulfil the Bragg condition for the (200) peak. The distance between the sample and detector was calibrated using LaB_6 powder, and the data was integrated using Saxsgui software. As the setup did not allow precise correction for the thermal dilatation of the stage, lattice parameter determination was not possible and hence the results were only used to observe changes in peak shape as a function of temperature. Due to significant instrumental broadening of the peaks, for these datasets the increase in the intensity was monitored rather than Full Width Half Maximum (FWHM).

Texture analyses experiments were performed on a D8 Discover (Bruker) equipped with a Cu X-ray source, a compact Eulerian cradle (Phi, Z, Chi), and Eiger 2D photon counting detector. Samples were aligned in the X-ray beam, and patterns were collected with varying Phi and Chi, up to 80°.

In situ NIR laser heating experiments were performed on the same D8 Discover with the laser placed within the enclosure of the instrument. Samples were placed on two 0.5 mm (outer diameter) glass capillaries with a wall thickness of 0.01 mm and aligned with the X-ray beam. The collimator of the laser system was placed 10 cm from the sample surface at a 90° angle, to ensure the whole sample was irradiated and that the irradiance was comparable between the

experiments. The support stage was designed to ensure that the NIR beam was not heating any elements in vicinity of the sample except the AuNRs. An overview image of the experimental setup is provided in Fig. 2. The peak evolution was monitored at each power plateau until no more changes were observed in the obtained diffraction patterns, typically 10-30 min depending on the laser power. Scan time was set to obtain satisfactory signal-to-noise ratio.

Collected data was analysed using EVA, TOPAS, and TEXTURE software from Bruker. The background was simulated with a Chebychev polynomial with between 1 to 3 coefficients. Diffraction peaks were fitted with a PearsonVII or Split PearsonVII function in TOPAS.

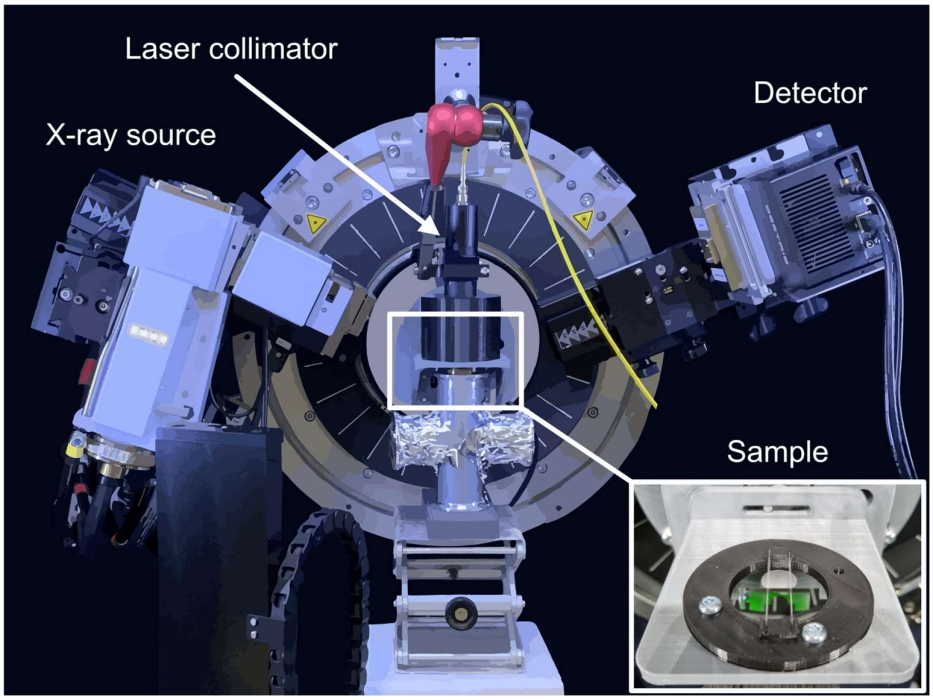

Fig. 2. Schematic illustration showing the experimental setup for the *in situ* XRD laser heating experiments, image insert showing the sample and sample holder.

3.4 Antibacterial activity

In Paper I, the antibacterial activity of the AuNR 3.9 supported on glass and titanium upon irradiation with NIR light was evaluated against *Staphylococcus aureus*, a bacterial species commonly found in BAIs [37]. Prior to the antibacterial activity evaluation, the samples were sterilised by UV/O_3-treatment for 5 min. For the *in vitro* studies, an agar plate model was developed to evaluate the antibacterial activity of the materials. In brief, *S. aureus* was inoculated in tryptic soy broth and incubated at 37 °C until it reached approximately 10^8 CFU/ml (determined by measuring the optical density). The bacterial inoculum was diluted with phosphate buffered saline (PBS) to a concentration of approximately 5×10^4 CFU/ml and then streaked onto brain heart infusion agar plates using cotton swabs. The samples were thereafter placed onto the agar plates with AuNR-functionalised side of the samples facing the bacteria. Non-functionalised glass and titanium substrates were used as controls.

Once placed on the agar plate, the samples were irradiated with the NIR laser. The glass samples were irradiated through the back, while the titanium samples that are not transparent to the NIR light were irradiated through the bottom of the agar plates. The sample placement on the agar plates and the irradiation order were randomised. A schematic illustration of the experimental setup is shown in Fig. 3. After NIR irradiation, the agar plates were incubated at 37 °C for 16 hours, whereafter the bacterial colonies on each sample were counted. To avoid growth from the perimeter of the samples to influence the quantification, colonies on the outmost 1 mm of the samples were excluded.

For the antibacterial activity evaluation, all sample groups were run in triplicates and the experiments were performed three times (n = 9). Statistical hypothesis testing was conducted using two-sample t-test assuming unequal variances. Significant differences in bar charts are indicated with letters. Two groups with the same letter indicates that there is no statistically significant difference between the means and two groups with different letters indicates that there is a statistically significant difference between the means.

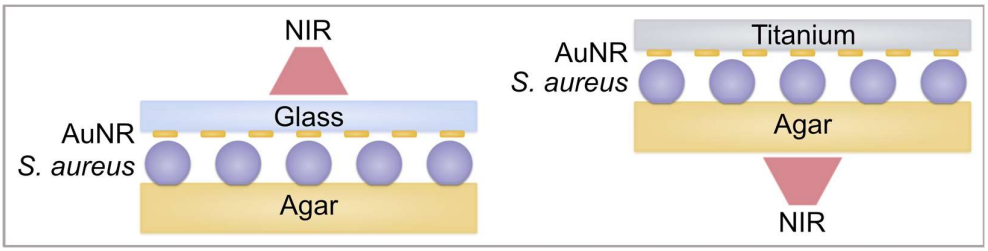

Fig. 3. Schematic illustration (not to scale) of the experimental setup used for NIR irradiation in the *in vitro* antibacterial activity evaluation.

4. Results and discussion

4.1 Material characterisation

4.1.1 Gold nanorods

The electrophoretic light scattering measurements performed in Paper I determined the electrophoretic mobility of the AuNR 3.9 to be 4.12 ± 0.07 μm·cm/Vs. From the electrophoretic mobility, the average zeta potential was calculated to be 52.9 mV using the Smoluchowski approximation. The positive zeta potential determined was expected of the CTAB-stabilised gold nanorods and indicated a sufficient colloidal stability of the nanoparticles. The DLS results were not used as a metric of particle size due to the limitations of DLS for non-spherical particles.

The synthesised AuNR suspensions had longitudinal plasmon resonance bands around 800-850 nm, with AuNR 3.9 exhibiting a maximum absorption at 825 nm, whereas the maximum for AuNR 4.4 was slightly red-shifted to 850 nm (Fig. 4A). The high shape purity of the synthesised AuNRs is indicated by the high relative intensity of the longitudinal resonance band compared to the transverse [38]. The 3.9 aspect ratio gold nanorods (Fig. 4B) exhibited a more dumbbell-shaped morphology compared to the straighter 4.4 aspect ratio gold nanorods (Fig. 4C). The two observed morphologies have been correlated to different stages in the growth process of the gold nanorods, wherein the dumbbell-shape occurs at an earlier stage before reshaping into straight nanorods later in the process [17,39]. It was thereby assumed that the utilised synthesis protocols arrested the growth of the gold nanorods at different growth stages, explaining the observed morphological differences.

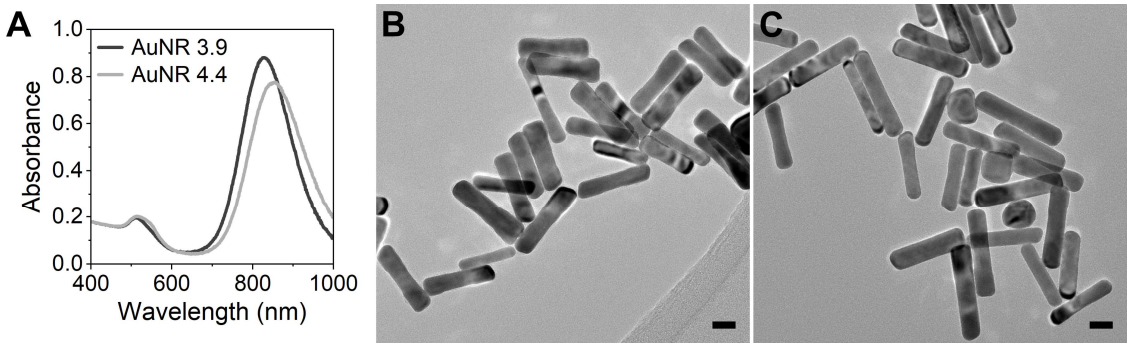

Fig. 4. (A) Absorption spectra of the synthesised gold nanorods. Overview TEM micrographs of the (B) 3.9 aspect ratio gold nanorods (AuNR 3.9) and (C) 4.4 aspect ratio gold nanorods (AuNR 4.4). Scale bars are 20 nm.

The dimensions of the synthesised AuNRs determined by measuring 400 particles in TEM micrographs are available in Table 1. The average dimensions of AuNR 3.9 were 67 x 18 nm, and of AuNR 4.4 66 x 15 nm.

Table 1. AuNR dimensions expressed as average ± standard deviation, determined from measuring 400 particles in TEM micrographs. For each particle the length, the width in the middle and the width of each end were measured. The values for "Width ends" are calculated from the average end width of each AuNR, and the values for "Width overall" are calculated from the average of all three widths measured. Aspect ratio = Length/Width overall.

	Length (nm)	Width middle (nm)	Width ends (nm)	Width overall (nm)	Aspect ratio
AuNR 3.9	67.2 ± 6.9	16.1 ± 2.0	18.4 ± 2.2	17.6 ± 2.1	3.9 ± 0.5
AuNR 4.4	66.0 ± 9.7	14.7 ± 2.2	15.3 ± 2.1	15.1 ± 2.1	4.4 ± 0.7

High-resolution TEM revealed the fcc single-crystalline structure of the gold nanorods (Fig. 5). In the TEM micrographs, clear lattice fringes could be observed with spacings in good agreement with the (200) planes in gold (0.203 nm) in parallel with and perpendicular to the growth direction of the AuNR (Fig. 5B and D). Spacings in fair agreement with the (110) planes in gold (0.287 nm) were also noted. Overall, the crystal structure of the gold nanorods was consistent with literature regarding gold nanorods synthesised in the presence of silver [40].

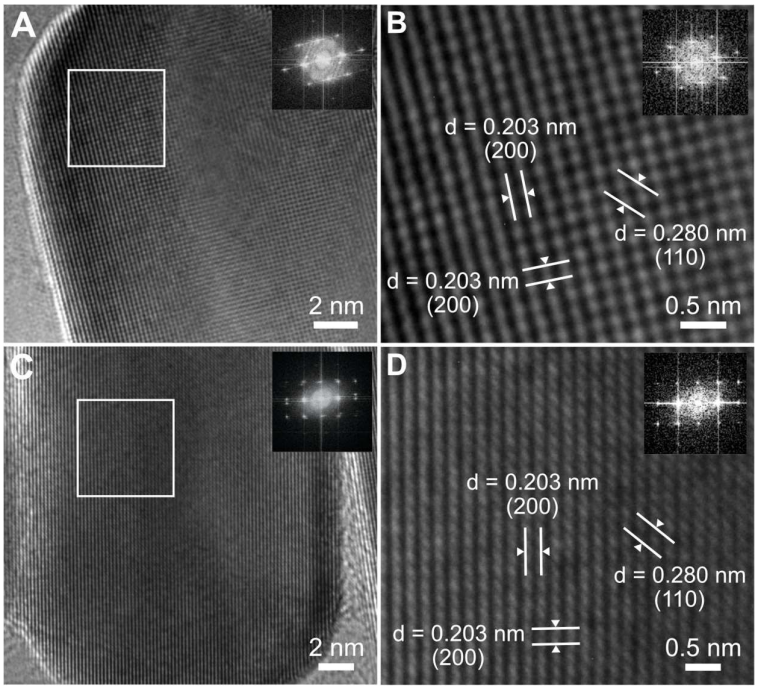

Fig. 5. High-resolution TEM micrographs of the synthesised gold nanorods with FFT inserts and lattice spacings indicated. (A) and (B) showing the 3.9 aspect ratio gold nanorods, (C) and (D) showing the 4.4 aspect ratio gold nanorods.

4.1.2 Gold nanorod-functionalised materials

In paper II, glass substrates were used as support for both AuNR 3.9 and AuNR 4.4 in the preparation of the samples for the *in situ* XRD experiments performed to evaluate the photothermal properties of the materials upon irradiation with NIR light. In paper I, both glass and titanium substrates functionalised with AuNR 3.9 were utilised, and the materials' antibacterial activity upon irradiation with NIR light was evaluated.

For the *in situ* XRD experiments in paper II, both the effect of the AuNR shape, a known parameter affecting their properties, and the collective heating were investigated. To this end, the two different morphologies of gold nanorods were immobilized onto glass substrates. Additionally, the collective heating was investigated by adjusting the surface coverage on the glass support. The three different samples of AuNRs supported on glass that were prepared are presented in Fig. 6. They include (1) AuNR 3.9 with an average surface coverage of 10.7% (Fig. 6A, AuNR 3.9 11%), (2) AuNR 3.9 with an average surface coverage of 13.4% (Fig. 6B, AuNR 3.9 13%), and (3) AuNR 4.4 with an average surface coverage of 11.0% (Fig. 6C, AuNR 4.4 11%). The absorption spectra of the samples in air (Fig. 6, inserts) revealed that the AuNRs retained their plasmonic properties when supported on glass. Compared to the AuNRs in aqueous suspension (Fig. 4A), a blue-shift of the longitudinal resonance bands to 775-825 nm was observed for the supported AuNRs. The shift was attributed to the change in refractive index of the medium surrounding the AuNRs associated with transitioning from aqueous suspension to the interface between glass and air. The longitudinal LSPR peak maxima overlapped well with the 808 nm NIR laser.

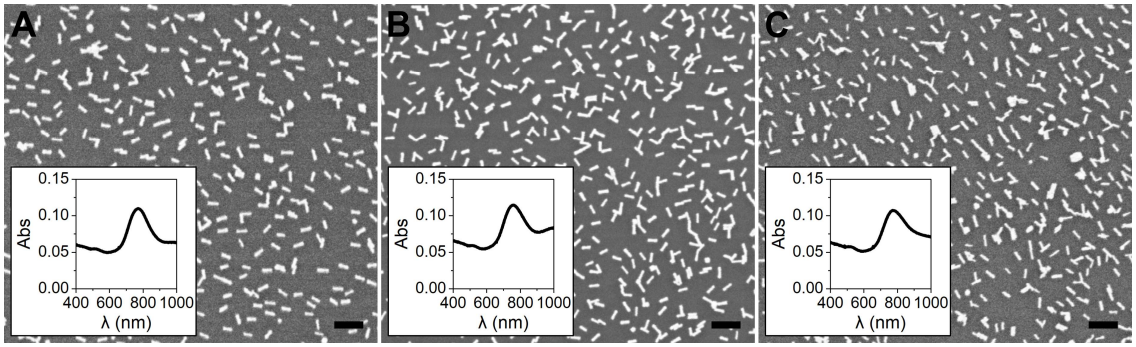

Fig. 6. SEM micrographs and UV-Vis spectra of AuNRs supported on glass. (A) AuNR 3.9 with an average surface coverage of 11%, (B) AuNR 3.9 with an average surface coverage of 13% and, (C) AuNR 4.4 with an average surface coverage of 11%. Scale bars are 200 nm.

For paper I, the AuNR 3.9 were immobilised onto glass and titanium substrates (Fig. 7). Measuring the absorption spectrum of the AuNR-functionalised glass immersed in water (Fig. 7A) showed that the particles retained their plasmonic properties. Compared to the AuNR 3.9 in aqueous suspension, a slight red-shift of the longitudinal LSPR peak maximum from 825 nm to 850 nm was observed. This shift was as well attributed to a change in refractive index of the medium surrounding the AuNR 3.9, but here due to transitioning from aqueous suspension to the interface between glass and water. The average surface coverages of the materials used in paper I were 13.7% for glass and 11.7% for titanium, which using the average dimensions of the AuNR 3.9, was estimated to 113 AuNR/μm^2 and 97 AuNR/μm^2, respectively.

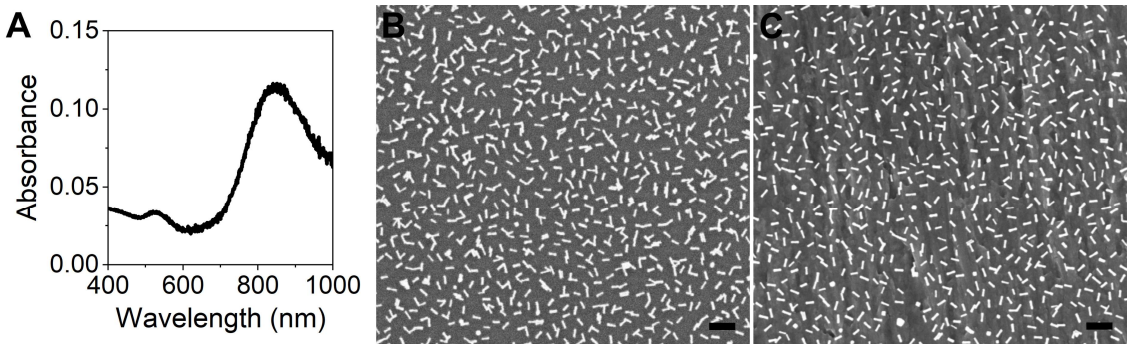

Fig. 7. (A) UV-Vis spectrum of AuNR-functionalised glass immersed in water. SEM micrographs of AuNR 3.9 on (B) glass and (C) titanium. Scale bars are 200 nm.

SEM characterisation showed that the electrostatic immobilisation procedures developed yielded even coverage of AuNRs on both glass (Fig. 6 and Fig. 7B) and titanium (Fig. 7C), where the AuNRs were attached in a well-defined manner without forming any larger aggregates. Bringing plasmonic nanoparticles in close proximity to one another will lead to interaction of their LSPR, known as plasmon coupling, causing a shift in the resonance frequency to occur. Here, the well-dispersed surface-immobilisation achieved allowed the AuNRs to largely retain their optical properties, with only small perturbation by plasmon coupling observable through the broadening of the longitudinal resonance peaks (Fig. 6 and Fig. 7A). The developed materials thus showed potential for achieving high photothermal efficiency at the NIR laser wavelength of 808 nm.

The procedures developed in paper I provide a straightforward approach for the surface-immobilisation of AuNRs on glass and titanium. By using suitable pre-conditioning of the substrates, successful and reproducible AuNR-functionalisation was achieved without requiring any additional linking molecule between the AuNRs and the support. Avoiding the use of linking molecules is beneficial for simplifying material preparation protocols and for preserving the surface chemistry of the biomaterial. On titanium, a simple activation by UV/O_3-treatment was enough to obtain the desired negative surface charge. However for glass, the pre-conditioning was shown to be of high importance. Before the final protocol using nitric acid (section 3.1.2) was established multiple procedures were evaluated, including functionalisation with (3-mercaptopropyl)trimethoxysilane, as well as pre-treating the substrates with basic piranha solution, with UV/O_3, and with oxygen plasma. Neither of said procedures yielded functionalisation as even and reproducible as the HNO_3 pre-treatment, which has been shown to reduce the amount of sodium, calcium, and aluminium cations on the surface of the glass [41], leaving behind a strongly negatively charged surface to which the positively charged AuNRs readily attach.

XPS was used to characterise the elemental composition of the AuNR-functionalised glass (Glass-AuNR) and titanium (Ti-AuNR) developed in paper I. Measurements were performed on untreated samples and on samples after the UV/O_3-treatment conducted as a sterilisation step prior to *in vitro* antibacterial activity evaluation. The survey spectra are shown in Fig. 8 and the quantified elemental composition in Table 2. The XPS measurements validated that the AuNRs constituted a minor part of the materials' surfaces as observed with SEM (Fig. 7A and B), shown by the few atomic percent of Au and Ag present. That the surface elemental

compositions of the materials' remain dominated by the chemical compositions of the substrates (here SiO_2 and Ti/TiO_2) is important when considering the aimed application as a biomaterial. By modifying a biomaterials' surface, its innate properties, like osseointegration for titanium, will be influenced. Therefore, it is desirable to design an antibacterial modification strategy that minimises altering the surface chemical composition of the biomaterial. After UV/O_3-treatment, a reduction in the amount of carbon could be observed (Table 2), indicating removal of CTAB from the surface-immobilised AuNRs. CTAB alone is toxic to cells at sub-micromolar concentrations, and though studies have shown that CTAB adsorbed onto gold nanoparticles have limited impact on cell viability [42,43], its removal remains important to minimise the risk of the AuNR-functionalised materials having detrimental impact on tissue cells.

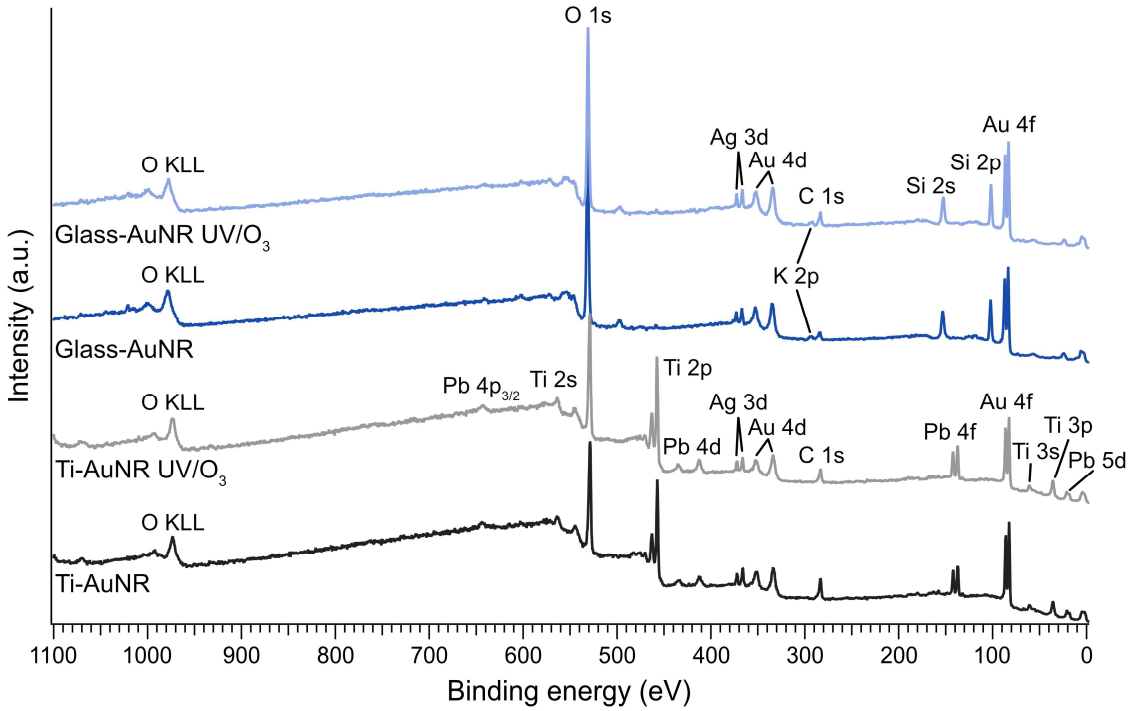

Fig. 8. X-ray photoelectron spectroscopy (XPS) survey spectra of Glass-AuNR and Ti-AuNR, with and without UV/O_3-treatment.

Table 2. Surface chemical composition in atomic percent of Glass-AuNR and Ti-AuNR with and without UV/O_3 treatment, determined with XPS.

	Atomic concentration %						
	C1s	O1s	Si2p	Ti2p	Br3d	Ag3d	Au4f
Glass-AuNR	10.61	62.01	22.49		0.31	0.82	3.75
Glass-AuNR UV/O_3	7.08	64.32	23.77		0.29	0.80	3.75
Ti-AuNR	23.49	53.68		17.17	0.37	0.97	4.31
Ti-AuNR UV/O_3	16.05	59.38		19.65	0.29	0.87	3.75

4.2 Evaluation of photothermal properties

4.2.1 Theory: heating of plasmonic nanoparticle arrays

The temperature increase of a perfect 2D array of individual plasmonic nanoparticles upon illumination with resonant light stem from two factors: (1) a self-temperature increase caused by heating of the NP (ΔT_0^s), and (2) an external temperature increase caused by heating from the surrounding NPs in the array (ΔT_0^{ext}), where the 0 subscript indicates the centre of the array. The relative contribution of the two can be expressed as a dimensionless parameter ζ_2 [44].

$$\zeta_2 = \frac{p^2}{3LR} \qquad \text{(Eq. 1)}$$

Where p is the interparticle distance, L the characteristic size of the irradiated area, and R the NP radius. When ΔT_0^s is dominant ($\zeta_2 >> 1$), the NPs exhibit a temperature increase that is unaffected by the neighbouring particles, meaning that the temperature increase is localised around each individual NP. When ΔT_0^{ext} is dominant ($\zeta_2 << 1$), the temperature increase of each NP is primarily due to heating of the neighbouring particles, i.e. collective heating dominates, and the temperature increase is delocalised with a smooth temperature distribution over the whole array. For the systems studied in paper II, ζ_2 was estimated to $\approx 10^{-5}$, and thus collective heating was predicted to dominate the photothermal properties of the materials.

The temperature increase of a regularly arranged 2D infinite NP array under uniform and circular irradiation can be estimated from summarising the self- and external heating of the system: [44]

$$\Delta T_0 = \Delta T_0^s + \Delta T_0^{ext} = \frac{\sigma_{abs} I}{4\pi\bar{\kappa}R} + \frac{\sigma_{abs} ID}{4\bar{\kappa}A}\left(1 - \frac{2\sqrt{A}}{\sqrt{\pi}D}\right) \qquad \text{(Eq. 2)}$$

Where σ_{abs} is the absorption cross-section of the NP, I the irradiance of the light source, $\bar{\kappa}$ the average thermal conductivity of the medium and substrate, R the NP radius, D the diameter of the heated area, and A the unit cell area of the NP array. For a square lattice $A = p^2$ and for hexagonal lattice $A = \sqrt{3}/2p^2$, where p is the interparticle distance. Although these models apply for perfect arrays of regularly arranged NPs, whereas the AuNR arrays studied in paper II were randomly arranged, they provide a qualitative understanding of the factors influencing the heating of the systems. From Eq. 2, a linear increase in temperature with laser power (given as irradiance, I, power per unit area) is expected, if the interparticle spacing and NP absorption cross-section are constant. Moreover, a greater temperature increase is expected with a smaller interparticle spacing ($A \propto p^2$), and thus an increase in surface coverage of AuNRs would result in a greater temperature increase for a set laser power.

4.2.2 *In situ* X-ray diffraction

In situ XRD was performed to evaluate the characteristics of the supported AuNRs during conventional furnace heating and NIR laser heating. The absence of the (111) peak in the Bragg-Brentano scan of a flat mounted sample demonstrate the strong orientation of the single crystal AuNRs supported on the glass, wherein only a broad (200) peak together with background from the glass substrates is observed (Fig. 9). Further texture analysis using a Eulerian cradle stage (Fig. 10) revealed that the majority of the AuNRs are single crystals, with

the (200) planes parallel to the longer axis and on the support, they are lying flat with the long edge on the glass substrate. The observed crystal structure correlates well with TEM characterisation (Fig. 5) and the orientation on the support is confirmed in the SEM micrographs (Fig. 6).

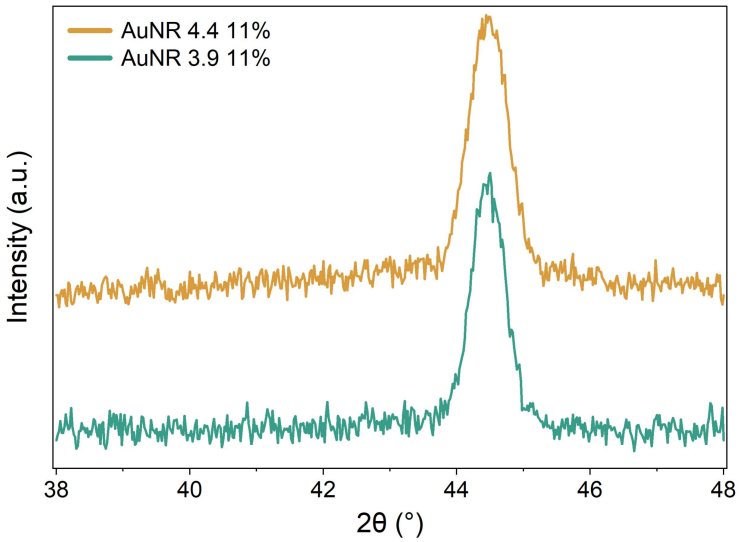

Fig. 9. XRD patterns of AuNR 3.9 11% and AuNR 4.4 11% with broad (200) peaks from the supported AuNRs.

By monitoring the position and shape of the (200) peak, the structure and morphology changes during heating can be followed. A series of *in situ* heating experiments were conducted on the samples discussed in section 4.1.2, firstly using conventional furnace heating, followed by NIR laser heating under constant illumination.

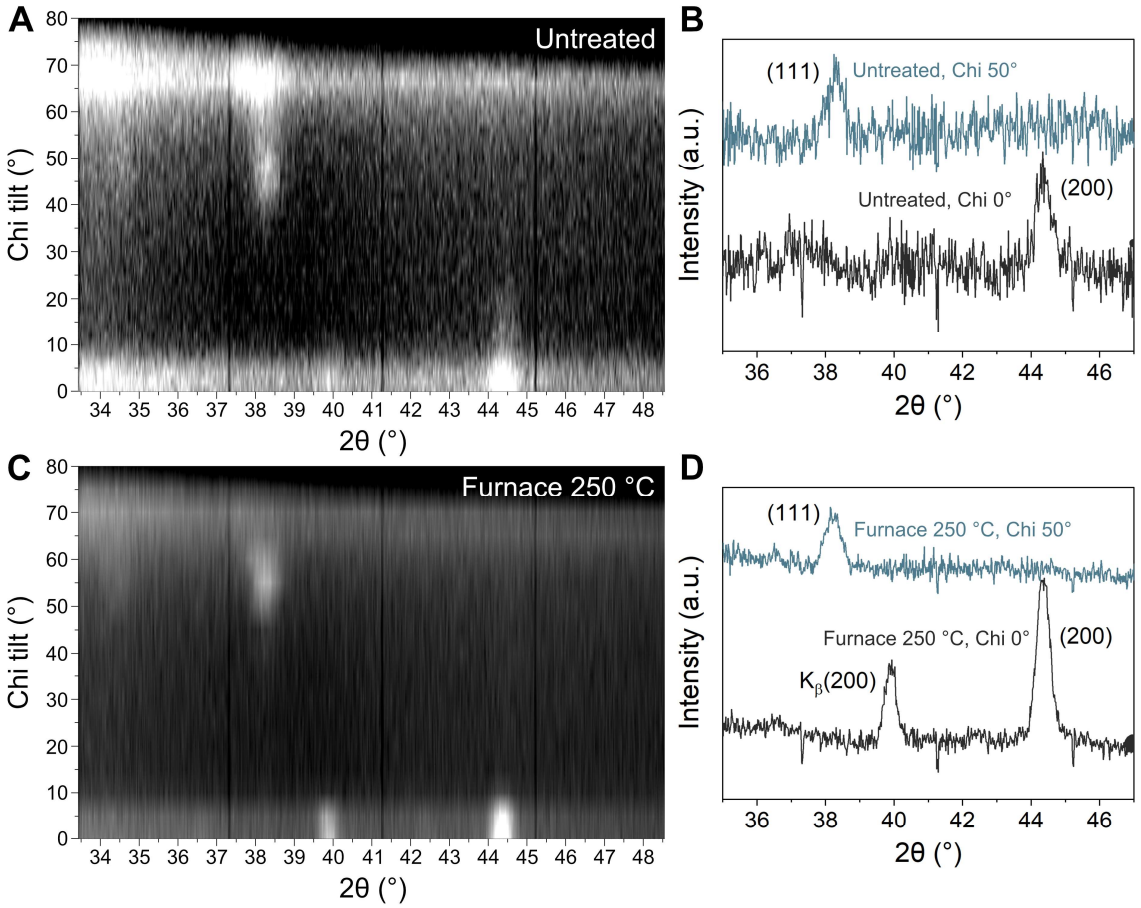

Fig. 10. Texture analysis of AuNR 3.9 11%. Intensity maps for an (A) untreated and (C) furnace heated (250 °C) sample. XRD patterns showing the (200) peak at Chi = 0° and (111) peak at Chi = 50° for an (B) untreated and (D) furnace heated (250 °C) sample.

4.2.2.1 Conventional heating

In Fig. 11 the lattice parameter, determined from the position of the (200) peak, as a function of the calibrated temperature for the AuNR 3.9 11% and AuNR 4.4 11% samples from conventional furnace heating in the XRK900 cell up to 150 °C is shown. Also included is the bulk lattice parameter, $\alpha_{gold}(T)$, as calculated from the thermal expansion coefficient for gold [45].

$$\alpha_{gold}(T) \times 10^6 = 12.00269 + 0.00953 \cdot \mathrm{T} - 8.4 \cdot 10^{-6} \cdot T^2 + 5.43 \cdot 10^{-9} \cdot T^3 \quad \text{(Eq. 3)}$$

In comparison to literature data for the thermal expansion of gold, the expansion coefficients of the AuNRs seem to be similar (within the limits of instrumental resolution). Fig. 11 also shows the evolution of Full Width Half Maximum (FWHM) of the (200) peak for the AuNR 4.4 11% sample, serving as a probe for morphological changes in the particles, where a decrease in FWHM is observed at the onset of morphological changes.

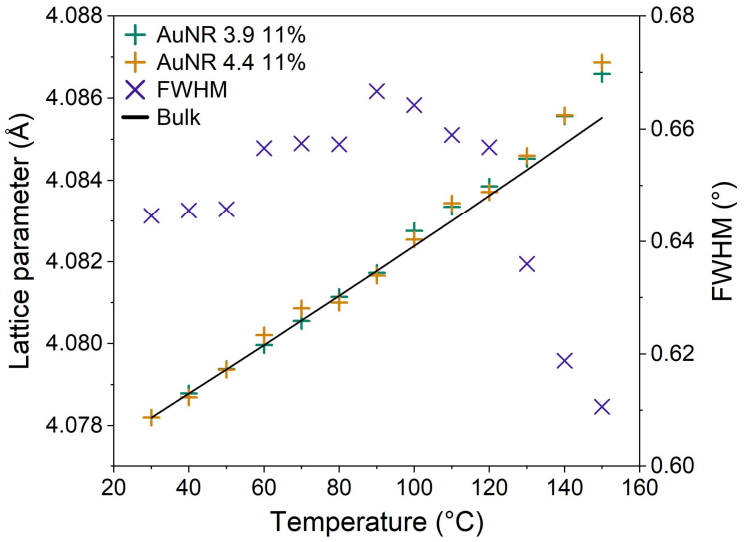

Fig. 11. Lattice parameter of the gold cubic structure together with Full Width Half Maximum (FWHM) plotted against temperature for AuNR 3.9 11% and AuNR 4.4 11%. The solid line represents the thermal expansion of bulk gold. The decrease in FWHM above 120 °C is attributed to morphological changes of the AuNRs.

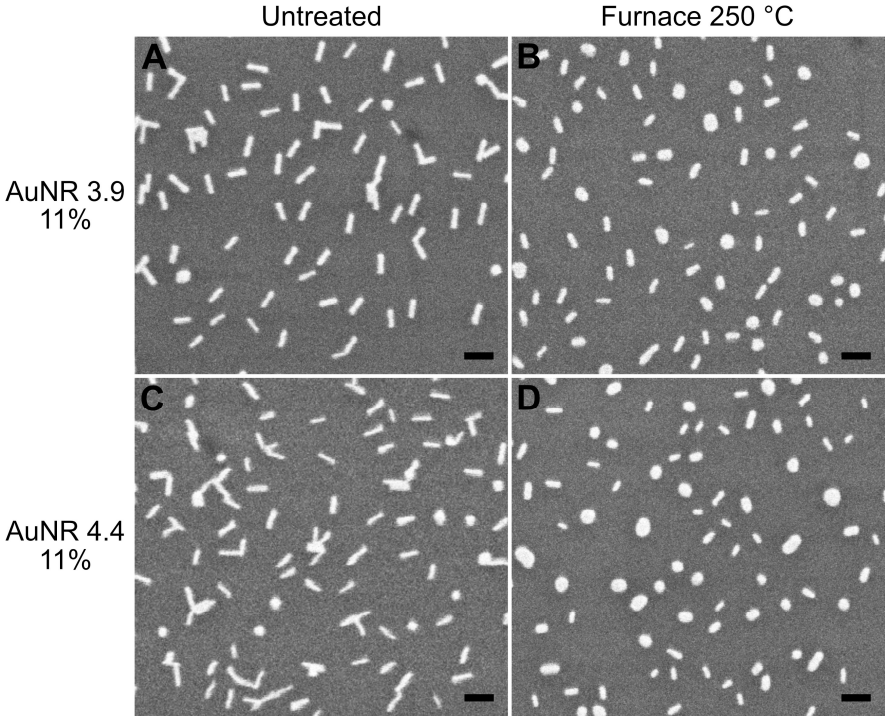

Fig. 12. SEM micrographs of AuNRs supported on glass. AuNR 3.9 11% (A) untreated, and (B) after furnace heating to 250°C. AuNR 4.4 11% (C) untreated, and (D) after furnace heating to 250°C. Scale bars are 100 nm.

Up to 100-120°C, the evolution of the (200) peak during heating is attributed to thermal expansion of the nanorods. Heating above 120°C introduces morphological changes, indicated by irreversible modification of the peak's shape. In the complementary heating experiments using a Linkam heating cell it was observed that the decrease in FWHM continues until at least 250 °C (details in paper II). SEM characterisation of the samples heated to 250 °C show a substantial reduction in the AuNRs aspect ratios, as well as coalescence of clusters of AuNRs into more spherical structures (Fig. 12). The morphological changes are also accompanied by prominent deviations in the UV-Vis absorption properties of the samples (Fig. 13A and B). Interestingly, the crystallite orientation of the particles is not affected by the morphological changes, shown by the continued absence of the (111) peak in the diffraction pattern after heating to 250 °C (Fig. 10D).

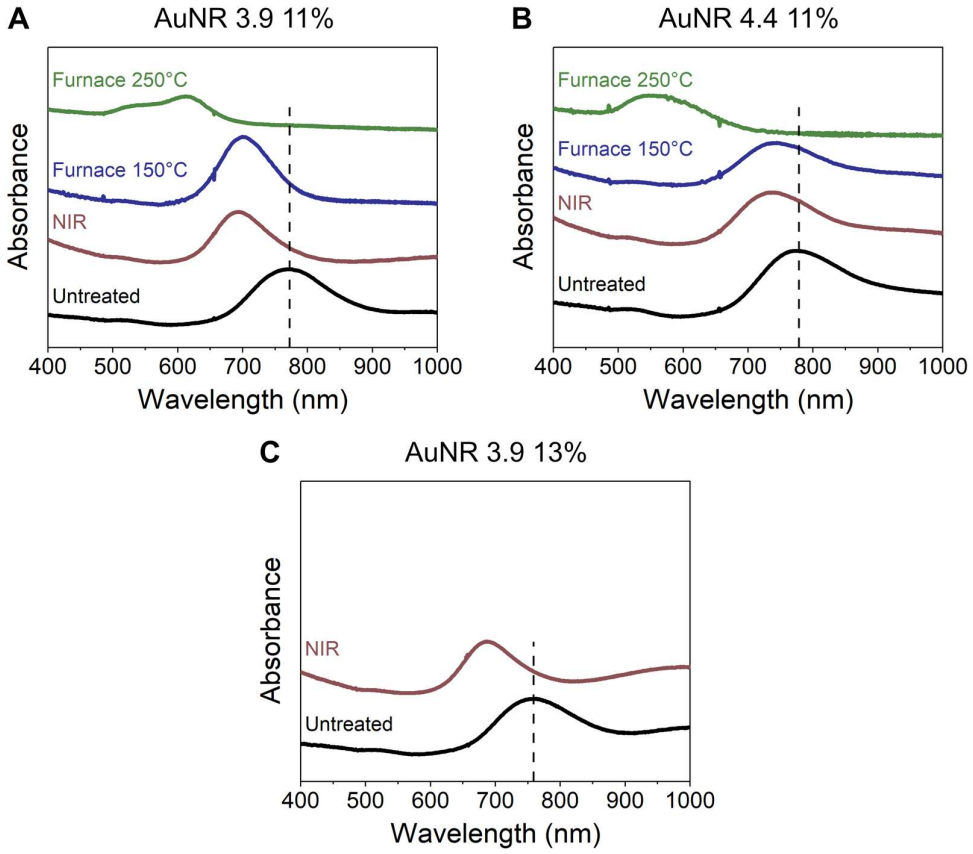

Fig. 13. UV-Vis absorption spectra of AuNR supported on glass. Spectra were obtained of untreated samples and of samples after the *in situ* XRD NIR laser and furnace heating experiments. (A) AuNR 3.9 11% (NIR up to 20 W), (B) AuNR 4.4 11% (NIR up to 24 W), and (C) AuNR 3.9 13% (NIR up to 24 W).

4.2.2.2 NIR laser heating

In the *in situ* NIR laser heating experiments, the samples were exposed to continuous NIR light at varying power up to 24 W and the thermal dilatation of the rods, resulting in a shift of the (200) peak to lower angles, was monitored. Similarly to the furnace heating experiments, a morphological evolution was observed. From comparing the measured thermal lattice expansion to literature values, a relation between the laser power and the temperature of the AuNRs in samples AuNR 3.9 11%, AuNR 3.9 13%, and AuNR 4.4 11% was established (Fig. 14). The AuNR 3.9 11% 24 W data point is missing due experimental setup failure.

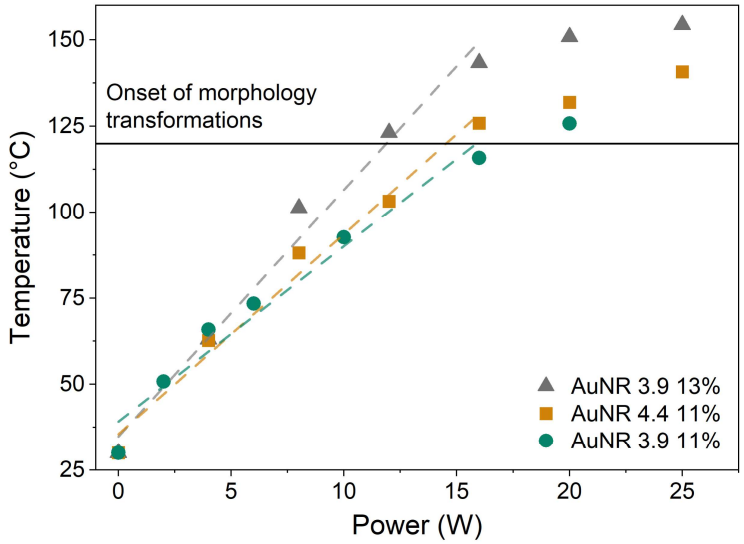

Fig. 14. Temperature as a function of laser power estimated from comparing the measured lattice parameters with bulk gold thermal expansion for samples AuNR 3.9 11%, AuNR 4.4 11% and AuNR 3.9 13%. Dashed lines represent linear trends up to 120 °C.

We observe a linear increase of the AuNRs' temperature with laser power until the onset of morphological changes around 120 °C, in line with the predictions made from the theoretical model presented in 4.2.1. Moreover, the slope of the linear trends increases with surface coverage, which also aligns well with the model. Increasing the average surface coverage from 10.7% to 13.4% for AuNR 3.9 yielded a corresponding 1.4-fold augmentation in the obtained temperature at a given power. The deviation from the linear trend observed above 120 °C can be explained by the morphological changes and the accompanying modification of the absorption properties of the AuNRs, shown by UV-Vis spectra of the NIR laser heated samples (Fig. 13). A blue-shift in the longitudinal LSPR peak can be observed, resulting in a lowering of the heating efficiency at 808 nm, eventually preventing further heating by increasing laser power. These observations are in line with the theoretical model, as morphological changes would result in variations in the AuNR radius (R) and absorption cross-section (σ_{abs}) in Eq. 2. No apparent difference between the two morphologies of AuNR (aspect ratio 3.9 and 4.4) could be discerned regarding the temperature reached for a given power. As collective heating seems to dominate for the supported AuNRs, as predicted by Eq. 1, it is feasible that the potentially small differences in R and σ_{abs} between the two AuNR morphologies have limited impact.

For the samples with 11% surface coverage of AuNRs, the peak intensity or FWHM did not change significantly above 12 W laser power but remained constant up to 24 W (details in paper II). Indications of morphological changes in these samples are the deviations from the linear trend in the temperature-power plot and the blue-shifts in the UV-Vis spectra obtained after NIR heating experiments (Fig. 13A and B). For the 13% coverage sample however, there was an obvious change in the peak shape upon NIR exposure of sufficient intensity, similarly to what was observed during conventional furnace heating. This discrepancy could potentially be linked to different level of clustering of the AuNRs in the 11% and 13% samples. SEM micrographs after furnace heating to 250 °C reveal that the clusters appear to have transformed into larger, more spherical structures, while the singular AuNRs have retained their rod-shape but with a decreased aspect ratio (Fig. 12). The two fractions of nanoparticles would contribute differently to the peak shape in the XRD patterns, wherein individual AuNRs would produce a relatively broad peak, while sharpening and possibly intensity increase would be expected from the larger, more spherical structures. A lower number of clusters in the 11% coverage samples and lower temperatures reached during NIR laser heating compared to the 13% coverage sample, could explain why we observed no discernible changes in the peak shape of the AuNR 3.9 11% and AuNR 4.4 11% samples during NIR illumination.

Based on the results from the *in situ* XRD studies, a precise correlation between the NIR laser power, exposure time, temperature of the AuNRs, and onset of morphological changes can be established. The findings give valuable insight for the practical application of the supported AuNRs for PTT and in the development of antibacterial biomaterial modifications. The observed onset of morphological changes of the AuNRs around 120 °C sets limitations on the temperature than can be achieved for therapeutic purposes without permanently changing the photothermal properties of the materials. The studies further show that by adjusting the surface coverage of AuNRs on the support, it is possible to tune the NIR laser power required to reach this temperature threshold.

4.3 Antibacterial activity

The antibacterial activity of the AuNR-functionalised materials upon irradiation with NIR light was evaluated against *S. aureus* as a function of laser intensity for 30 s irradiation time. The evaluation was performed using an agar plate model, wherein samples were placed with the AuNR-functionalised side down onto bacterial-covered agar plates, irradiated with NIR light, and after incubation, the number of colonies on the samples counted. Bare titanium (Ti) and glass (Glass) samples were used as control.

4.3.1 Gold nanorod-functionalised titanium

From the *in vitro* antibacterial activity evaluation of the AuNR-functionalised titanium (Fig. 15) a significant antibacterial activity was observed for both Ti and Ti-AuNR irradiated at 10 W/cm^2 for 30 s, compared with all other sample groups. As no significant antibacterial activity was observed for the non-irradiated Ti-AuNR, the AuNR-functionalisation in itself did not influence bacterial viability. Irradiating the Ti-AuNR at 10 W/cm^2 resulted in an 82.1% reduction in bacterial viability compared to the non-irradiated Ti-AuNR (average CFU/cm^2 values compared). However, no significant difference was observed compared to the Ti

irradiated with the same irradiance. Moreover, the Ti irradiated at 10 W/cm^2 exhibited at 70.9% reduction in bacterial viability compared to the non-irradiated Ti. For the lower irradiance evaluated of 5 W/cm^2, no significant antibacterial effect was shown for Ti or T-AuNR.

The results from the *in vitro* antibacterial activity evaluation showed that when using titanium as the support for the AuNRs, no significant antibacterial effect caused by photothermal heating of the AuNRs could be discerned. The antibacterial activity observed could instead be

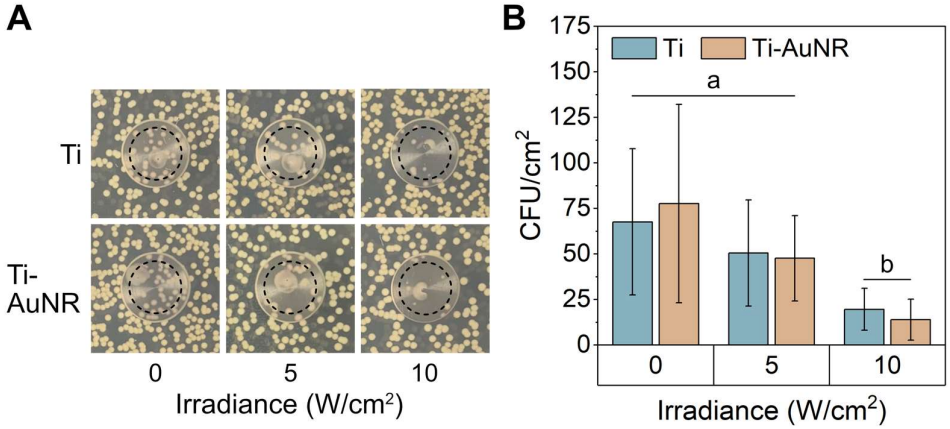

Fig. 15. Antibacterial activity against *S. aureus* of Ti-AuNR irradiated with NIR light for 30 s of different irradiances (0 = non-irradiated, 5 and 10 W/cm^2. (A) Showing example pictures from the agar plate model with bacterial colonies appearing as yellow dots and the black dashed circles indicate the sampling area, and (B) data expressed as CFU/cm^2 (n=9). Significance level: $p < 0.05$.

correlated to the laser irradiance used during NIR exposure, where at a high enough intensity (10 W/cm^2) a significant reduction in viable bacteria was noted for both Ti and Ti-AuNR. The antibacterial effect was therefore attributed to NIR light absorption of the titanium, which has a high optical extinction coefficient at 808 nm, resulting in bulk heating of the substrate. This assumption is further corroborated by the fact that titanium is established to have plasmon damping properties, wherein the disruption of the plasmon resonance stems from titanium's dielectric function, which introduces absorption and affects the refractive index locally [46,47].

4.3.2 Gold nanorod-functionalised glass

From the *in vitro* antibacterial activity evaluation of the AuNR-functionalised glass (Fig. 16) a significant antibacterial activity was observed for the Glass-AuNR irradiated at 20 W/cm^2 for 30 s, compared to all other sample groups. The Glass-AuNR irradiated at 20 W/cm^2 showed a 99.1% reduction in viable bacteria compared to the non-irradiated Glass-AuNR, and a 99.2% reduction compared to the Glass control exposed to the same irradiance (average CFU/cm^2 values compared). For the lower irradiances evaluated, 5 and 10 W/cm^2, no significant antibacterial effect was observed for the Glass-AuNR irradiated with NIR light, showing the clear laser intensity-dependency of the antibacterial effect. No significant antibacterial activity could be noted for the non-irradiated Glass-AuNR, indicating that the AuNR-functionalisation in itself did not influence bacterial viability. It furthermore highlights the light-activated nature of the antibacterial effect observed.

As the glass substrates are transparent to NIR light, the antibacterial activity observed for the Glass-AuNR irradiated at 20 W/cm^2 can be attributed to plasmonic heating of the AuNRs. This is further validated by the lack of antibacterial activity observed for the irradiated Glass control, showing that the laser intensity itself did not influence bacterial viability. The local nature of the photothermal antibacterial effect is emphasised by the clear bacterial growth observed outside the illuminated area (Fig. 16A). Obtaining a local effect is of relevance as it is desirable to develop a modification strategy that effectively can combat bacterial colonisation, while simultaneously having minimal detrimental effects on surrounding tissue.

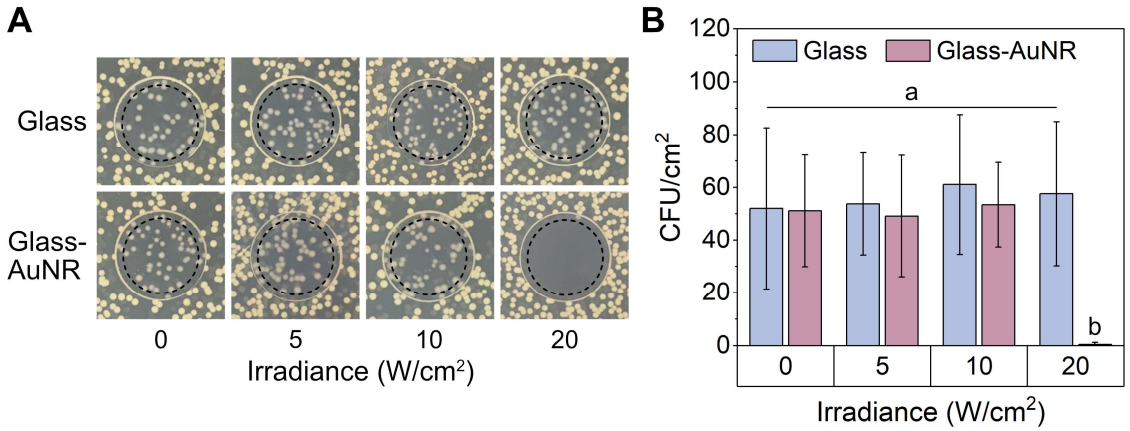

Fig. 16. Antibacterial activity against *S. aureus* of Glass-AuNR irradiated with NIR light for 30 s of different irradiances (0 = non-irradiated, 5, 10 and 20 W/cm^2. (A) Showing example pictures from the agar plate model with bacterial colonies appearing as yellow dots and the black dashed circles indicate the sampling area, and (B) data expressed as CFU/cm^2 (n=9). Significance level: $p < 0.001$.

The SEM micrographs from the antibacterial activity evaluation in Fig. 17 were taken at the edges of the colonies visible in Fig. 16A, where the number of bacteria were few enough to visualise the underlying substrate, for the samples were this was relevant. The micrographs in Fig. 17A-C for samples Glass, Glass 20 W/cm^2 and Glass-AuNR respectively, show the formation of bacterial biofilms on the sample surfaces. In contrast, for Glass-AuNR irradiated at 20 W/cm^2 (Fig. 17D) no biofilm formation occurred, and only small clusters of bacterial cells could be observed at a few locations. The large difference in bacterial load on the samples correlate well with the quantified antibacterial activity in Fig. 16. SEM characterisation moreover revealed the AuNR-functionalisation to be largely unaffected after the *in vitro* antibacterial activity evaluation (inserts in Fig. 17C and D).

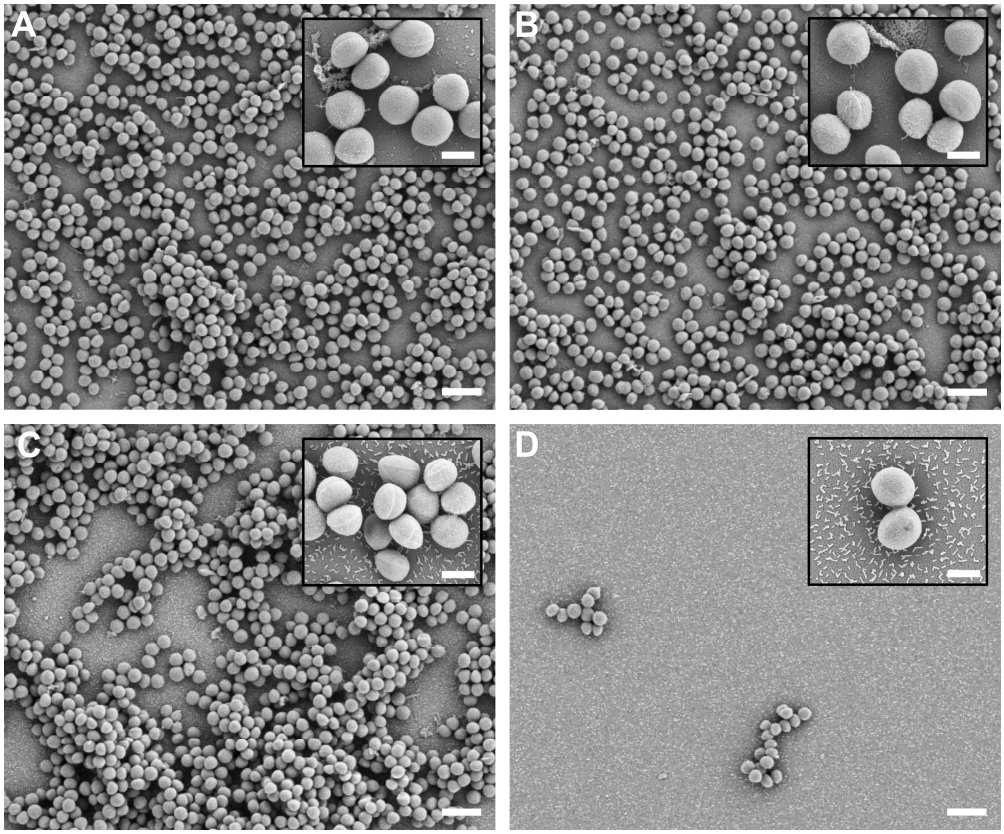

Fig. 17. SEM micrographs samples from the antibacterial activity evaluation against *S. aureus* of Glass-AuNR irradiated with NIR light of different irradiances. The samples shown being (A) Glass, (B) Glass irradiated at 20 W/cm^2 for 30 s, (C) Glass-AuNR, and (D) Glass-AuNR irradiated at 20 W/cm^2 for 30 s. The low and high (insert) magnification scale bars are 2 μm and 500 nm, respectively.

In our study, a clear antibacterial efficacy was observed for glass functionalised with around 100 AuNR/μm^2 (12-13% projected area coverage), compared to previous studies where material coverages ranging from a few hundred nanoparticles per μm^2 to complete multilayer coatings on the surfaces can be found [8,23–26]. The AuNR loading required to obtain an antimicrobial effect is an important aspect, as ideally the modification should not impede the innate tissue-interactive properties of the biomaterial to any significant extent. By employing high AuNR loadings, the innate properties of the biomaterial will undoubtedly be affected. Moreover, tightly packed or clustered AuNRs will interact through plasmon coupling, resulting in alteration of their optical properties and thereby impact on the photothermal efficiency. The well-dispersed surface-immobilisation achieved here allowed the AuNRs to retain their optical properties with minimum perturbation by plasmon coupling. Simultaneously, the low loading of AuNRs allowed the surface elemental composition to be dominated by the chemical composition of the substrate. Taken together with the clear antibacterial activity observed at sufficient NIR light intensities, the AuNR-functionalisation developed shows promise as an effective antibacterial modification strategy that minimises impact on the biomaterial's innate properties.

5. Concluding remarks

This thesis focused on the use of supported gold nanorods and near-infrared light for the development of photothermal antibacterial biomaterial modifications. Straightforward and reproducible material preparation procedures for the surface-immobilisation of AuNRs on glass and titanium have been developed, and the properties of the materials were evaluated. The two main focus areas were evaluating the photothermal properties of the AuNRs supported on glass with *in situ* X-ray diffraction (paper II), and investigating the *in vitro* antibacterial activity of the AuNRs supported on titanium and glass (paper I).

From the results of the *in situ* XRD studies, a correlation between the NIR laser power, temperature of the AuNRs, and the onset of morphological changes could be established. In accordance with the referenced theoretical model for periodic nanoparticle arrays, we observed that the temperature of the AuNRs' increased linearly with laser power within a certain temperature range. The slope of the temperature-power profile demonstrated a dependence on the AuNR surface coverage, thus providing a way of tuning the photothermal behaviour of the systems. Within the accuracy of our methodology, no differences in how the AuNRs responded to NIR laser heating and conventional furnace heating were discerned. An onset of morphological changes in the AuNRs was observed at 120 °C, far below the melting temperature of bulk gold. SEM imaging of post-experiment samples revealed the morphological changes to include a decrease in aspect ratio of individual AuNRs and coalescence of clustered AuNRs. The changes were accompanied by a blue-shift in the longitudinal LSPR peaks, shown in the UV-Vis spectra of post-experiment samples, motivating the deviation from the linear temperature-power profile observed in the NIR laser heating experiments. The findings give valuable insights into the photothermal properties of supported AuNRs, critical for their practical application in antibacterial biomaterial modifications.

From the evaluation of the antibacterial activity of gold nanorods immobilised on titanium and glass upon NIR light irradiation against *S. aureus*, a clear discrepancy between the two support materials was demonstrated. A laser intensity-dependent antibacterial activity was observed for both materials, however a significant difference in the origin of the effect could be noted. For titanium, the antibacterial activity was attributed to NIR light absorption by the substrate leading to heating of the samples, with no evident effects from plasmonic heating of the AuNRs. However on glass, a significant antibacterial activity attributed to local plasmonic heating of the AuNRs was observed. The developed modification strategy thus showed a clear antibacterial effect on glass, while only introducing minor alterations to the surface chemical composition of the support, showing promise for retention of the biomaterial's innate properties. The results are importance for advancing the design of antibacterial biomaterial modifications using gold nanorods and NIR light, and for deepening our understanding of the interactions between nanomaterials, biomaterials, and bacteria.

6. Future perspectives

As revealed from the *in situ* XRD studies, the temperature-power profile from the NIR laser heating experiments were dependent on the surface coverage of AuNRs on the support. Further investigations into how this dependency behaves by examining additional surface coverages would be of great interest to deepen our understanding of the systems. Additionally, performing TEM characterisation of the post-experiment AuNRs could reveal more detailed information on morphological changes induced by the NIR laser and conventional furnace heating, and shed light on potential effects on the AuNRs' crystal structure.

Regarding the antibacterial activity of gold nanorods on titanium, it would be of interest to investigate whether an effect from plasmonic heating of AuNRs could be achieved by tuning the system further, possibly by introducing a spacer or coating between the titanium substrate and the AuNRs, which could reduce the influence of plasmon damping [46,47]. Furthermore, extending the modification strategy to additional biologically relevant support materials would be of significant importance, furthering the investigation of how the material influences the antibacterial activity of the supported AuNRs.

For the gold nanorods on glass which exhibited a significant antibacterial activity from plasmonic heating upon irradiation with NIR light, *in vitro* cytotoxicity evaluations need to be conducted to evaluate the biocompatibility of the developed modification strategy. By extension, future investigations on how the materials perform *in vivo* using an animal infection model would be of great relevance.

Acknowledgements

The Area of Advance in Materials Science at Chalmers University of Technology and the Knut and Alice Wallenberg Foundation through the Wallenberg Academy Fellow program is acknowledged for financial support.

I would like to thank my supervisor Martin Andersson for your guidance and encouragement. Your endless output of new ideas and positive mindset have been immensely valuable throughout the past years. To my co-supervisor Mats Hulander, for your support and for always believing in me. Thank you for all your help and all the interesting discussions, they have been a true source of inspiration and motivation. To my examiner, Andreas Dahlin, thank you for your time and effort in my PhD education.

To my co-authors, Michal Strach, Gustav Eriksson and Tetiana Dmytrenko, I have really enjoyed working on these projects together and hope we can continue with new ones in the future. To Andreas Schaefer, a big thanks for your help with XPS measurements.

To all the members in MA research group, current and past. A special thank you to Edvin, Annija and Gustav, for always being willing to help out and for being such fantastic company on this journey. To everyone at the Applied Chemistry division, for making it such an enjoyable place to work.

To my family and friends, for the happiness and encouragement. Finally, I would like to thank my boyfriend David, for your love and endless support.

Maja Uusitalo
Gothenburg, April 2024

References

[1] World Health Organization, World health statistics 2023: monitoring health for the SDGs Sustainable Development Goals, Geneva, 2023.

[2] M. Vert, Y. Doi, K.H. Hellwich, M. Hess, P. Hodge, P. Kubisa, M. Rinaudo, F. Schué, Terminology for biorelated polymers and applications (IUPAC recommendations 2012), Pure and Applied Chemistry 84 (2012) 377–410. https://doi.org/10.1351/PAC-REC-10-12-04.

[3] W. Zimmerli, Clinical presentation and treatment of orthopaedic implant-associated infection, J Intern Med 276 (2014) 111–119. https://doi.org/10.1111/joim.12233.

[4] H.J. Busscher, H.C. Van Der Mei, G. Subbiahdoss, P.C. Jutte, J.J.A.M. Van Den Dungen, S.A.J. Zaat, M.J. Schultz, D.W. Grainger, Biomaterial-associated infection: Locating the finish line in the race for the surface, Sci Transl Med 4 (2012). https://doi.org/10.1126/scitranslmed.3004528.

[5] N. Høiby, T. Bjarnsholt, M. Givskov, S. Molin, O. Ciofu, Antibiotic resistance of bacterial biofilms, Int J Antimicrob Agents 35 (2010) 322–332. https://doi.org/10.1016/j.ijantimicag.2009.12.011.

[6] C.J. Murray, K.S. Ikuta, F. Sharara, L. Swetschinski, G. Robles Aguilar, A. Gray, C. Han, C. Bisignano, P. Rao, E. Wool, S.C. Johnson, A.J. Browne, M.G. Chipeta, F. Fell, S. Hackett, G. Haines-Woodhouse, B.H. Kashef Hamadani, E.A.P. Kumaran, B. McManigal, R. Agarwal, S. Akech, S. Albertson, J. Amuasi, J. Andrews, A. Aravkin, E. Ashley, F. Bailey, S. Baker, B. Basnyat, A. Bekker, R. Bender, A. Bethou, J. Bielicki, S. Boonkasidecha, J. Bukosia, C. Carvalheiro, C. Castañeda-Orjuela, V. Chansamouth, S. Chaurasia, S. Chiurchiù, F. Chowdhury, A.J. Cook, B. Cooper, T.R. Cressey, E. Criollo-Mora, M. Cunningham, S. Darboe, N.P.J. Day, M. De Luca, K. Dokova, A. Dramowski, S.J. Dunachie, T. Eckmanns, D. Eibach, A. Emami, N. Feasey, N. Fisher-Pearson, K. Forrest, D. Garrett, P. Gastmeier, A.Z. Giref, R.C. Greer, V. Gupta, S. Haller, A. Haselbeck, S.I. Hay, M. Holm, S. Hopkins, K.C. Iregbu, J. Jacobs, D. Jarovsky, F. Javanmardi, M. Khorana, N. Kissoon, E. Kobeissi, T. Kostyanev, F. Krapp, R. Krumkamp, A. Kumar, H.H. Kyu, C. Lim, D. Limmathurotsakul, M.J. Loftus, M. Lunn, J. Ma, N. Mturi, T. Munera-Huertas, P. Musicha, M.M. Mussi-Pinhata, T. Nakamura, R. Nanavati, S. Nangia, P. Newton, C. Ngoun, A. Novotney, D. Nwakanma, C.W. Obiero, A. Olivas-Martinez, P. Olliaro, E. Ooko, E. Ortiz-Brizuela, A.Y. Peleg, C. Perrone, N. Plakkal, A. Ponce-de-Leon, M. Raad, T. Ramdin, A. Riddell, T. Roberts, J.V. Robotham, A. Roca, K.E. Rudd, N. Russell, J. Schnall, J.A.G. Scott, M. Shivamallappa, J. Sifuentes-Osornio, N. Steenkeste, A.J. Stewardson, T. Stoeva, N. Tasak, A. Thaiprakong, G. Thwaites, C. Turner, P. Turner, H.R. van Doorn, S. Velaphi, A. Vongpradith, H. Vu, T. Walsh, S. Waner, T. Wangrangsimakul, T. Wozniak, P. Zheng, B. Sartorius, A.D. Lopez, A. Stergachis, C. Moore, C. Dolecek, M. Naghavi, Global burden of bacterial antimicrobial resistance in 2019: a systematic analysis, The Lancet 399 (2022) 629–655. https://doi.org/10.1016/S0140-6736(21)02724-0.

[7] D. Campoccia, L. Montanaro, C.R. Arciola, A review of the biomaterials technologies for infection-resistant surfaces, Biomaterials 34 (2013) 8533–8554. https://doi.org/10.1016/j.biomaterials.2013.07.089.

[8] Y.Q. Zhao, Y. Sun, Y. Zhang, X. Ding, N. Zhao, B. Yu, H. Zhao, S. Duan, F.J. Xu, Well-Defined Gold Nanorod/Polymer Hybrid Coating with Inherent Antifouling and

Photothermal Bactericidal Properties for Treating an Infected Hernia, ACS Nano 14 (2020) 2265–2275. https://doi.org/10.1021/acsnano.9b09282.

[9] X. Huang, P.K. Jain, I.H. El-Sayed, M.A. El-Sayed, Plasmonic photothermal therapy (PPTT) using gold nanoparticles, Lasers Med Sci 23 (2008) 217–228. https://doi.org/10.1007/s10103-007-0470-x.

[10] J.B. Vines, J.H. Yoon, N.E. Ryu, D.J. Lim, H. Park, Gold nanoparticles for photothermal cancer therapy, Front Chem 7 (2019). https://doi.org/10.3389/fchem.2019.00167.

[11] R. Weissleder, A clearer vision for in vivo imaging, Nat Biotechnol 19 (2001) 316–317.

[12] V. Amendola, R. Pilot, M. Frasconi, O.M. Maragò, M.A. Iatì, Surface plasmon resonance in gold nanoparticles: A review, Journal of Physics Condensed Matter 29 (2017). https://doi.org/10.1088/1361-648X/aa60f3.

[13] M. Faraday, The Bakerian Lecture: Experimental Relations of Gold (and Other Metals) to Light, Philos Trans R Soc Lond 147 (1857) 145–181. https://about.jstor.org/terms.

[14] P.K. Jain, X. Huang, I.H. El-Sayed, M.A. El-Sayed, Noble metals on the nanoscale: Optical and photothermal properties and some applications in imaging, sensing, biology, and medicine, Acc Chem Res 41 (2008) 1578–1586. https://doi.org/10.1021/ar7002804.

[15] X. Huang, S. Neretina, M.A. El-Sayed, Gold nanorods: From synthesis and properties to biological and biomedical applications, Advanced Materials 21 (2009) 4880–4910. https://doi.org/10.1002/adma.200802789.

[16] J. Kimling, M. Maier, B. Okenve, V. Kotaidis, H. Ballot, A. Plech, Turkevich method for gold nanoparticle synthesis revisited, Journal of Physical Chemistry B 110 (2006) 15700–15707. https://doi.org/10.1021/jp061667w.

[17] L. Scarabelli, A. Sánchez-Iglesias, J. Pérez-Juste, L.M. Liz-Marzán, A "Tips and Tricks" Practical Guide to the Synthesis of Gold Nanorods, Journal of Physical Chemistry Letters 6 (2015) 4270–4279. https://doi.org/10.1021/acs.jpclett.5b02123.

[18] X. Huang, I.H. El-Sayed, W. Qian, M.A. El-Sayed, Cancer cell imaging and photothermal therapy in the near-infrared region by using gold nanorods, J Am Chem Soc 128 (2006) 2115–2120. https://doi.org/10.1021/ja057254a.

[19] E.B. Dickerson, E.C. Dreaden, X. Huang, I.H. El-Sayed, H. Chu, S. Pushpanketh, J.F. McDonald, M.A. El-Sayed, Gold nanorod assisted near-infrared plasmonic photothermal therapy (PPTT) of squamous cell carcinoma in mice, Cancer Lett 269 (2008) 57–66. https://doi.org/10.1016/j.canlet.2008.04.026.

[20] R. Sean Norman, J.W. Stone, A. Gole, C.J. Murphy, T.L. Sabo-Attwood, Targeted photothermal lysis of the pathogenic bacteria, pseudomonas aeruginosa, with gold nanorods, Nano Lett 8 (2008) 302–306. https://doi.org/10.1021/nl0727056.

[21] Y. Zhao, Q. Guo, X. Dai, X. Wei, Y. Yu, X. Chen, C. Li, Z. Cao, X. Zhang, A Biomimetic Non-Antibiotic Approach to Eradicate Drug-Resistant Infections, Advanced Materials 31 (2019). https://doi.org/10.1002/adma.201806024.

[22] G. Baffou, F. Cichos, R. Quidant, Applications and challenges of thermoplasmonics, Nat Mater 19 (2020) 946–958. https://doi.org/10.1038/s41563-020-0740-6.

[23] T. Yang, D. Wang, X. Liu, Assembled gold nanorods for the photothermal killing of bacteria, Colloids Surf B Biointerfaces 173 (2019) 833–841. https://doi.org/10.1016/j.colsurfb.2018.10.060.

[24] I. De Miguel, I. Prieto, A. Albornoz, V. Sanz, C. Weis, P. Turon, R. Quidant, Plasmon-Based Biofilm Inhibition on Surgical Implants, Nano Lett 19 (2019) 2524–2529. https://doi.org/10.1021/acs.nanolett.9b00187.

[25] Y. Zhu, M. Ramasamy, D.K. Yi, Antibacterial activity of ordered gold nanorod arrays, ACS Appl Mater Interfaces 6 (2014) 15078–15085. https://doi.org/10.1021/am503153v.

[26] M. Pihl, E. Bruzell, M. Andersson, Bacterial biofilm elimination using gold nanorod localised surface plasmon resonance generated heat, Materials Science and Engineering C 80 (2017) 54–58. https://doi.org/10.1016/j.msec.2017.05.067.

[27] S. Freddi, L. Sironi, R. D'Antuono, D. Morone, A. Donà, E. Cabrini, L. D'Alfonso, M. Collini, P. Pallavicini, G. Baldi, D. Maggioni, G. Chirico, A molecular thermometer for nanoparticles for optical hyperthermia, Nano Lett 13 (2013) 2004–2010. https://doi.org/10.1021/nl400129v.

[28] G. Baffou, M.P. Kreuzer, F. Kulzer, R. Quidant, Temperature mapping near plasmonic nanostructures using fluorescence polarization anisotropy, Opt Express 7 (2009) 3291–3298. https://doi.org/https://doi.org/10.1364/OE.17.003291.

[29] S. Rohani, M. Quintanilla, S. Tuccio, F. De Angelis, E. Cantelar, A.O. Govorov, L. Razzari, F. Vetrone, Enhanced Luminescence, Collective Heating, and Nanothermometry in an Ensemble System Composed of Lanthanide-Doped Upconverting Nanoparticles and Gold Nanorods, Adv Opt Mater 3 (2015) 1606–1613. https://doi.org/10.1002/adom.201500380.

[30] H. Ma, P.M. Bendix, L.B. Oddershede, Large-scale orientation dependent heating from a single irradiated gold nanorod, Nano Lett 12 (2012) 3954–3960. https://doi.org/10.1021/nl3010918.

[31] P.M. Bendix, S.N.S. Reihani, L.B. Oddershede, Direct measurements of heating by electromagnetically trapped gold nanoparticles on supported lipid bilayers, ACS Nano 4 (2010) 2256–2262. https://doi.org/10.1021/nn901751w.

[32] G. Baffou, P. Bon, J. Savatier, J. Polleux, M. Zhu, M. Merlin, H. Rigneault, S. Monneret, Thermal imaging of nanostructures by quantitative optical phase analysis, ACS Nano 6 (2012) 2452–2458. https://doi.org/10.1021/nn2047586.

[33] D. Andrén, L. Shao, N. Odebo Länk, S.S. Aćimović, P. Johansson, M. Käll, Probing Photothermal Effects on Optically Trapped Gold Nanorods by Simultaneous Plasmon Spectroscopy and Brownian Dynamics Analysis, ACS Nano 11 (2017) 10053–10061. https://doi.org/10.1021/acsnano.7b04302.

[34] L. Jauffred, A. Samadi, H. Klingberg, P.M. Bendix, L.B. Oddershede, Plasmonic Heating of Nanostructures, Chem Rev 119 (2019) 8087–8130. https://doi.org/10.1021/acs.chemrev.8b00738.

[35] A. Plech, V. Kotaidis, S. Grésillon, C. Dahmen, G. Von Plessen, Laser-induced heating and melting of gold nanoparticles studied by time-resolved x-ray scattering, Phys Rev B Condens Matter Mater Phys 70 (2004). https://doi.org/10.1103/PhysRevB.70.195423.

[36] D.F. Wong, K. Young, Y.S. Ng, A. Plech, S. Kürbitz, K.-J. Berg, H. Graener, G. Berg, S. Grésillon, M. Kaempfe, J. Feldmann, M. Wulff, G. Von Plessen, Time-resolved X-ray diffraction on laser-excited metal nanoparticles, Europhys. Lett 61 (2003) 762–768.

[37] C.R. Arciola, D. Campoccia, P. Speziale, L. Montanaro, J.W. Costerton, Biofilm formation in Staphylococcus implant infections. A review of molecular mechanisms and implications for biofilm-resistant materials, Biomaterials 33 (2012) 5967–5982. https://doi.org/10.1016/j.biomaterials.2012.05.031.

[38] N.R. Jana, Gram-scale synthesis of soluble, near-monodisperse gold nanorods and other anisotropic nanoparticles, Small 1 (2005) 875–882. https://doi.org/10.1002/smll.200500014.

[39] K. Park, L.F. Drummy, R.C. Wadams, H. Koerner, D. Nepal, L. Fabris, R.A. Vaia, Growth mechanism of gold nanorods, Chemistry of Materials 25 (2013) 555–563. https://doi.org/10.1021/cm303659q.

[40] M. Liu, P. Guyot-Sionnest, Mechanism of silver(I)-assisted growth of gold nanorods and bipyramids, Journal of Physical Chemistry B 109 (2005) 22192–22200. https://doi.org/10.1021/jp054808n.

[41] H.K. Jang, Y.D. Chung, S.W. Whangbo, T.G. Kim, C.N. Whang, S.J. Lee, S. Lee, Effects of chemical etching with nitric acid on glass surfaces, Journal of Vacuum Science & Technology A: Vacuum, Surfaces, and Films 19 (2001) 267–274. https://doi.org/10.1116/1.1333087.

[42] A.M. Alkilany, P.K. Nagaria, C.R. Hexel, T.J. Shaw, C.J. Murphy, M.D. Wyatt, Cellular uptake and cytotoxicity of gold nanorods: Molecular origin of cytotoxicity and surface effects, Small 5 (2009) 701–708. https://doi.org/10.1002/smll.200801546.

[43] E.E. Connor, J. Mwamuka, A. Gole, C.J. Murphy, M.D. Wyatt, Gold nanoparticles are taken up by human cells but do not cause acute cytotoxicity, Small 1 (2005) 325–327. https://doi.org/10.1002/smll.200400093.

[44] G. Baffou, P. Berto, E. Bermúdez Ureña, R. Quidant, S. Monneret, J. Polleux, H. Rigneault, Photoinduced heating of nanoparticle arrays, ACS Nano 7 (2013) 6478–6488. https://doi.org/10.1021/nn401924n.

[45] Y.S. Touloukian, Y.B. Kirby, R.E. Taylor, P.D. Desai, Thermal expansion: metallic elements and alloys, in: Thermophysical Properties of Matter, IFI/Plenum, New York, 1975.

[46] T. Siegfried, Y. Ekinci, O.J.F. Martin, H. Sigg, Engineering metal adhesion layers that do not deteriorate plasmon resonances, ACS Nano 7 (2013) 2751–2757. https://doi.org/10.1021/nn4002006.

[47] T.G. Habteyes, S. Dhuey, E. Wood, D. Gargas, S. Cabrini, P.J. Schuck, A.P. Alivisatos, S.R. Leone, Metallic adhesion layer induced plasmon damping and molecular linker as a nondamping alternative, ACS Nano 6 (2012) 5702–5709. https://doi.org/10.1021/nn301885u.